MIT Libraries | DSpace@MIT

MIT Open Access Articles

Experiment and simulation validated analytical equivalent circuit model for piezoelectric micromachined ultrasonic transducers

Massachusetts Institute of Technology

Experiment and Simulation Validated Analytical Equivalent Circuit Model for Piezoelectric Micro-Machined Ultrasonic Transducer

Katherine Smyth and Sang-Gook Kim

Abstract

An analytical Mason equivalent circuit is derived for a circular, clamped plate piezoelectric micro-machined ultrasonic transducer (pMUT) design in 31 mode considering an arbitrary electrode configuration at any axisymmetric vibration mode. The explicit definition of lumped parameters based entirely on geometry, material properties and defined constants enables straightforward and wide ranging model implementation for future pMUT design and optimization. Beyond pMUTs, the acoustic impedance model is developed for universal application to any clamped, circular plate system and operating regimes including relevant simplifications are identified via the wave number-radius product ka. For the single electrode fundamental vibration mode case, sol-gel $Pb\left(Zr_{0.52}\right)Ti_{0.48}O_3$ (PZT) pMUT cells are micro-fabricated with varying electrode size to confirm the derived circuit model with electrical impedance measurements. For the first time, experiment and finite element simulation results are successfully applied to validate extensive electrical, mechanical and acoustic analytical modeling of a pMUT cell for wide ranging applications including medical ultrasound, non-destructive testing, and range finding.

I. INTRODUCTION

In recent years, thin film piezoelectric micro-machined ultrasonic transducers (pMUTs) have garnered attention for a wide variety of applications including range finding [1], non-destructive testing (NDT), object detection [2], and medical applications [3], [4]. Although significant advances have been achieved with bulk systems, the labor intensive manufacturing process restrains the realization of cost effective, small form factor and 2D arrays for advanced imaging [5]. As an alternative, micro-electromechanical system (MEMS) based designs show promise for cost-effective manufacturability at large volume of miniaturized elements and improved performance via novel actuation and sensing mechanisms made possible by small length scales.

In medical imaging, capacitive micro-machined transducer (cMUT) technology has garnered well-deserved attention for $\approx 100\%$ yield, $> 100\%$ bandwidth, and small form factor elements that have successfully been integrated with CMOS integrated circuits into fully operational 3D real time imaging systems [6]–[8]. Compared to traditional bulk transducer technology, cMUTs have already demonstrated significant resolution improvements for superficial imaging; however, low acoustic power results in diminished performance with increased depth [9]. Unfortunately, requirements for electrostatic actuation including small gap height, large bias voltage, and inherent non-linear transduction [10] act to reduce potential acoustic power, create safety concerns, and introduce significant circuit design challenges, respectively.

For high acoustic pressure output, the high energy density of piezoelectrics compared to other MEMS transduction mechanisms [11] makes piezoelectric MUTs a viable MEMS based alternative for increasingly sensitive, high depth ultrasound. Despite achievements in pMUT research [1], [3], [4], [12]–[18], predictive modeling and optimization capabilities are limited in improving reduced effective electromechanical coupling k_{eff}^2 and bandwidth in fabricated devices. In the most mature recent projects, fabricated pMUT designs are based heavily on geometry specific finite element models [19] with analytical models commonly limited to resonant frequency determination [4], [16], [20], [21]. A lack of available models leading to performance shortcomings demonstrate a need for more robust, fundamental understanding of pMUT performance.

Some work has begun to address the analytical model gap by focusing on the development of plate theory based electromechanical models [1], [3], [13], [22]–[28]. In [3], [22], explicit analytical equations for effective electromechanical coupling k_{eff}^2 are defined based on material constants and geometric parameters enabling

optimized design for high k_{eff}^2. More comprehensive approaches [1], [13], [23]–[27] expand model capabilities to include definitions of lumped mechanical and electrical impedance parameters of the Mason equivalent circuit. Although accurate, most of these models are complicated or implicitly defined making the full scale circuit model difficult to practically implement [13], [23], [24].

With developed analytical models, electrode size optimization performed for high k_{eff}^2 and deflection [3], [26], [28], [29] demonstrates the usefulness of analytical approaches for more flexible, straight-forward performance optimization via tailored geometry. In support of some analytical modeling endeavors, finite element models have been successfully implemented [22]–[27]. However, analytical approaches have yet to be proven by experiment because of discrepancies commonly attributed to residual stress [1], [3], [25], [29]. For an analytical model useful to future pMUT design, the model must be extensively confirmed with experimental results and use relevantly simplified lumped parameters for ease of use in design optimization. For practicality, analytical models should focus on the Mason model equivalent circuit, which directly sets bandwidth, k_{eff}^2, transmit and receive sensitivity, and power amplification circuit requirements [30].

Building on a previously discussed Green's function deflection model for a 31 mode unimorph pMUT [28], we present a general, analytical Mason equivalent circuit model of an arbitrary electrode and axisymmetric mode system. The model explicitly defines electrical, mechanical and acoustic domain parameters based on geometry, material properties, and defined mode constants. For the first time, measurements from fabricated PZT thin film based pMUTs and finite element model data are employed to comprehensively validate the analytical Mason equivalent circuit model. In experiment, plate-mode vibration of pMUT devices is demonstrated through mode shape measurements, an accurate method for extracting the piezoelectric constant based on static deflection is introduced, and a direct, iterative fit technique for electrical impedance measurements is implemented. Using these developed tools, experimental results and simulation data strongly validate the air loaded lumped parameters applicable to NDT and range finding applications. Further, finite element simulation supported results are discussed for expansion to fluid loaded systems relevant to medical ultrasound. Finally, appropriate lumped parameter simplifications are introduced based on average values and limiting cases of the physical system to facilitate future design optimization.

NOMENCLATURE

2β	motional impedance angle
ϵ_{33}^{σ}	dielectric constant measured at constant stress
ϵ_0	vacuum permittivity
γ	frequency dependent plate vibration parameter
γ_{0n}	axisymmetric vibration mode constant normalized to plate radius
λ	wavelength
Λ_{0n}	deflection profile constant
λ_{0n}	axisymmetric vibration mode constant
μ	angular coordinate in acoustic radiation
ν_i	poisson ratio of layer i
ω	angular frequency
Ψ_{0n}	characteristic shape profile at axisymmetric mode n
$\Psi_{avg,11}$	shape profile averaged over single electrode area
ρ	density of fluid medium
$\varepsilon_{rr}, \varepsilon_{\theta\theta}$	tensor strain in polar coordinates
a	plate radius
a_k''	outer radius of electrode k
a_k'	inner radius of electrode k
a_e	single electrode outer radius
A_{0n}	deflection amplitude at axisymmetric mode n
a_{exp}	experimental plate radius
B_{nk}	dimensionless coupling between electrode k and axisymmetric vibration mode n
b_n	axisymmetric mode n depedent mechanical impedance constant
C	total mechanical compliance

c	speed of sound in fluid medium
C_p	parasitic capacitance
$C_{0,k}$	fixed, shunt capacitance at electrode k
$C_{f,k}$	free capacitance at electrode k
$C_{m,n}$	mechanical compliance at axisymmetric vibration mode n
D	flexural rigidity
D_3	out of plane electrical displacement
d_{31}	piezoelectric constant
E_3	electric field in z
$e_{31,f}$	transverse piezoelectric constant
F	out of plane force
f	frequency
f', f''	half power frequencies
f_0	resonant frequency of fundamental mode
f_a	anti-resonant frequency
$f_{0,n}$	resonant frequency of higher order axisymmetric modes
G_0	static piezoelectric conductance
g_{0n}	Hankel transform of shape profile function related to beam pattern at axisymmetric vibration mode n
h_i	thickness of ith layer
i	material layer index
I_0	surface density
I_3	out of plane current
I_{nk}	out of plane current at electrode k and axisymmetric mode n
j	$\sqrt{-1}$
k	electrode index
k	wave number
$k_{2_{31}}$	planar material electromechanical coupling
K_n	directivity at axisymmetric mode n
k_{eff}^2	effective electromechanical coupling constant
$K_{m,Mason}$	mechanical stiffness approximation by Mason
$K_{m,n}$	mechanical stiffness at axisymmetric vibration mode n
K_{rp}	directivity of rigid piston
ka	dimensionless acoustic parameter
L	total mechanical and acoustic inductance
$L_{m,Mason}$	mechanical inductance approximation by Mason
$L_{m,n}$	mechanical inductance at axisymmetric vibration mode n
$L_{r,n}$	acoustic radiation inductance at axisymmetric vibration mode n
M	static deflection slope
M_p	piezoelectrically induced bending moment
MLR	empirical mechanical loss ratio
N	total number of electrodes or total transformation ratio
n	axisymmetric vibration mode index
N'	total transformation ratio normalized to transverse piezoelectric constant
N_n	electromechanical transformation ratio at axisymmetric vibration mode n
p	piezoelectric layer index
P_ω	applied pressure
q	total number of material layers
Q_m	mechanical quality factor
R	total electrical resistance or total mechanical and acoustic resistance
R_e	static electrical resistance
$R_{m,n}$	acoustic radiation resistance at axisymmetric vibration mode n

$r_{r,n}$	dimensionless radiation resistance at axisymmetric mode n
u_{nk}	average out of plane plate velocity at electrode k and axisymmetric vibration mode n
V	Voltage
W	deflection in z
$W_{avg,11}$	deflection averaged over single electrode area
W_{nk}	radially dependent out of plane deflection at electrode k and axisymmetric mode n
X	total electrical reactance
X_e	static electrical reactance
$x_{r,n}$	dimensionless radiation reactance at axisymmetric mode n
Y_i	Young's modulus of layer i
Z_e	neutral plane under applied electric field
z_i	material stack thickness at i^{th} layer
z_N	neutral plane
Z_p	piezoelectric moment arm
$z_{m,n}$	mechanical impedance at axisymmetric mode n
$Z_{r,n}$	acoustic radiation impedance at axisymmetric mode n

II. MODEL

Previously, we derived an analytical solution for the deflection of a unimorph piezoelectric micro-machined transducer plate design [28] using a Green's function approach. The structure of unimorph pMUT is the 31 piezoelectric mode: the electrical field is applied perpendicular to the surface across the thickness of the PZT film between a top and grounded bottom electrode to generate in-plane stress to deflect the diaphragm as shown in Figure 1.
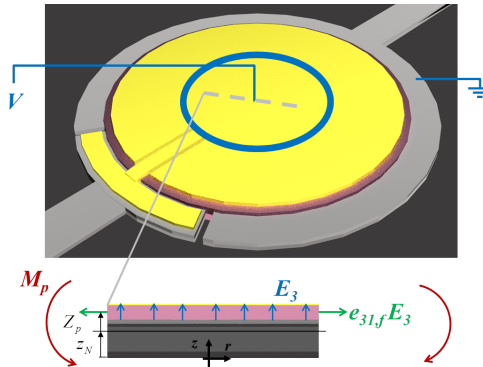

Fig. 1. Single electrode, first axisymmetric vibration mode in transmit case. Rendered image of fabricated single electrode pMUT cell with electrical routing showing 31-mode actuation mechanism. Alternating current electric field applied in the 3-direction creates transverse stress $e_{31,f}E_3$ at a distance Z_p from the neutral plane z_N inducing a bending moment M_p that causes plate mode vibrations. Fabricated dimensions shown in Table I and fabrication process discussed in Section IV.

TABLE I
MEASURED DIMENSIONS OF FABRICATED pMUTs

Layer*	Thickness h (μm)
1: Buried Oxide	1
2: Si	3.5
3: Thermal Oxide	0.2
4: Ti	0.03
5: Pt	0.2
6 (p): PZT	0.275
7: Ti	0.03
8: Au	0.175

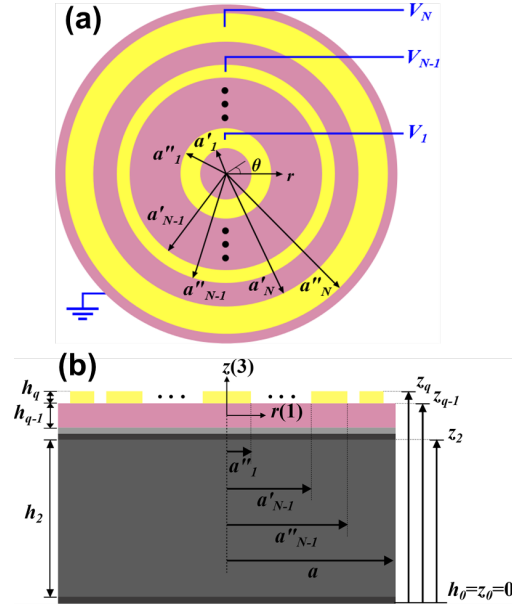*Numbering of material layers corresponds to notation in Figure 2b.

Fig. 2. Top (a) and cross-section (b) schematic of N electrode pMUT consisting of q material layers. Stack thickness z_i determined by thickness of ith layer h_i and preceding layers according to Appendix A.

For a plate excited by an alternating current source of angular frequency $\omega = 2\pi f$, the governing plate vibration equation dependent on the the amplitude of pressure P_ω, piezoelectric moment M_p and deflection W in z is given by:

$$\left(\nabla^4 - \gamma^4\right) W = \frac{1}{D}\left(\nabla^2 M_p + P_\omega\right) \tag{1}$$

where D, the flexural rigidity of the plate, represents a stiffness term [28]. Here, γ is frequency dependent parameter related to mass and stiffness as:

$$\gamma^4 = \frac{\omega^2 I_0}{D} \tag{2}$$

where I_0 is the surface density or mass per unit area (see Appendix A).

Plate vibrations are induced via the applied piezoelectric moment M_p resulting from a voltage V_k applied across electrode k with inner radius a_k' and outer radius a_k'':

$$M_p = e_{31,f} Z_p \sum_{k=1}^{N} V_k \left(H\left(r - a_k'\right) - H\left(r - a_k''\right)\right) \tag{3}$$

4

where $e_{31,f}$ is the modified transverse piezoelectric constant. A schematic of the general multiple circular/ring pMUT system is shown in Figure 2. The piezoelectric moment is applied at a distance Z_p referencing the neutral plane z_N as depicted in Figure 1b and defined in Equation 11.

Under no applied moment or force in the homogeneous solution case, the characteristic function that defines the deflection profile at axisymmetric mode $(0, n)$:

$$\Psi_{0n}(r) = J_0(\gamma_{0n}r) - \frac{J_0(\gamma_{0n}a)}{I_0(\gamma_{0n}a)}I_0(\gamma_{0n}r) \tag{4}$$

To satisfy the clamped plate boundary condition, the solution depends on γ_{0n}, which is conventionally defined as the axisymmetric mode constant λ_{0n} normalized to the plate radius a [31]:

$$\gamma_{0n} = \frac{\lambda_{0n}}{a} \tag{5}$$

The mode shape constant along with material parameters also sets the resonant frequency:

$$f_{0,n} = \frac{\lambda_{0n}^2}{2\pi a^2}\sqrt{\frac{D}{I_0}} \tag{6}$$

Since resonant frequency is an easily measured property, the definition in Equation 6 is useful for verifying that the material and thickness parameters used for calculating D and I_0 before input into the deflection model.

In the previous derivation [28], the externally applied pressure was neglected; however, for the equivalent circuit, this applied force term is necessary to determine coupling between the electrical and mechanical domain. As such, an updated Green's function based solution is constructed piece-wise from the previously derived piezoelectric moment dependent form and the pressure dependent term:

$$W(r_0) = \frac{e_{31,f}Z_p}{D}\sum_n^N\sum_{k=1}\frac{V_k}{\Lambda_{0n}(\gamma_{0n}^4 - \gamma^4)}\Psi(r_0)B_{nk} + \frac{P_\omega}{D}\sum_n^N\sum_{k=1}\frac{1}{\Lambda_{0n}(\gamma_{0n}^4 - \gamma^4)}\left[\frac{2aJ_1(\lambda_{0n})}{\lambda_{0n}}\right]\Psi(r_0) \tag{7}$$

represented by the first and second terms of Equation 7, respectively (see <mark>Appendix B</mark> for more detail on Green's function approach). Here, the design dependent constant B_{nk} is introduced as:

$$B_{nk} = \gamma_{0n}\left[a_k'\left(J_1(\gamma_{0n}a_k') + \frac{J_0(\lambda_{0n})}{I_0(\lambda_{0n})}I_1(\gamma_{0n}a_k')\right) - a_k''\left(J_1(\gamma_{0n}a_k'') + \frac{J_0(\lambda_{0n})}{I_0(\lambda_{0n})}I_1(\gamma_{0n}a_k'')\right)\right] \tag{8}$$

B_{nk} is a dimensionless measure of the coupling between electrode k and axisymmetric vibration mode n and typically varies between 0 and 1. For maximized deflection, electrode coverage should be optimized to most effectively couple with the vibration mode of interest. In our previous work [28], deflection was maximized through a single electrode with radial coverage of $\approx 60\%$. A plot of the coupling constant B_{11} shown in Figure 3 agrees with this approach, showing that the $\approx 60\%$ radial coverage is ideal for coupling between a single electrode and the first axisymmetric vibration mode.

III. EQUIVALENT CIRCUIT

In linearized equivalent circuit network form, the Mason model is commonly used to represent transducer systems [32]. The most general theoretical representation for a 31 mode pMUT resonating near axisymmetric mode n excited by a voltage applied at electrode k is shown in Figure 4 and based on the form presented in [33]. For application to experiment, the specific case of a single electrode at the fundamental resonant mode is provided in Figure 5a and shows non-idealities in a real system including dielectric loss, mechanical damping, and parasitic capacitance. For equivalent circuit model fitting, the Mason equivalent circuit is further lumped to take the form of the Butterworth Van Dyke (BVD) circuit as shown in Figure 5b.
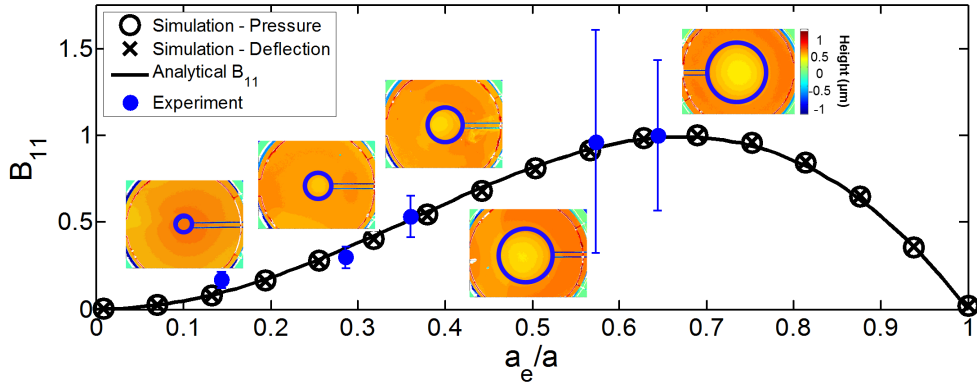
Fig. 3. Dimensionless electrode radial coverage plotted against the coupling constant B_{11}. For one electrode, coupling between electrode size and the first axisymmetric vibration mode is maximized for electrode radius of $\approx 60\%$. Simulations of a pMUT device at resonance in oil confirm the scaling of output pressure with deflection. Non-dimensionalized experimental and simulated values of pressure and deflection follow B_{11} prediction. Experimental B_{11} determined from static deflection as described in Section V-B. Insets show raw surface profilometer data for $a = 139.5 \pm 0.2\mu m$ devices at $V_{DC} = 7V$ with area used for deflection averaging outlined.
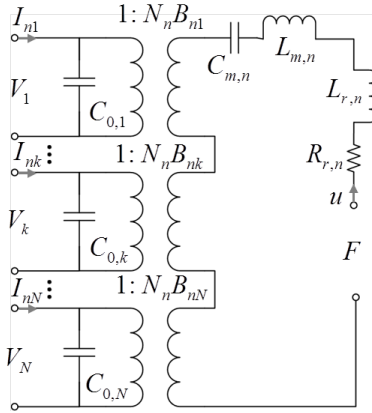

Fig. 4. General Mason equivalent circuit of arbitrary circular/ring N electrode structure excited at axisymmetric mode n. Voltage V_k applied at electrode k. Lumped mechanical capacitance $C_m = 1/K_m$.
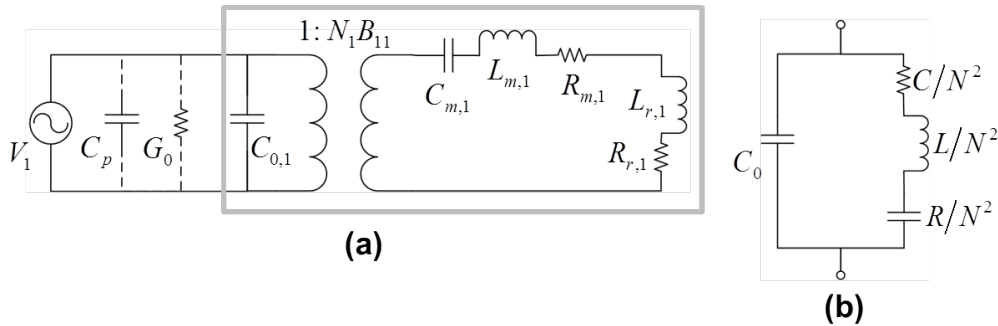

Fig. 5. Single electrode, first axisymmetric vibration mode transmit case equivalent circuit including static conductance G_0 and parasitic capacitance C_p with Mason model in (a) and Butterworth Van Dyke representation in (b). Parameters defined as $C_0 = C_{0,1}$, $N = N_1 B_{11}$, $L = L_{m,1} + L_{r,1}$, $C = C_{m,1}$, and $R = R_{m,1} + R_{r,1}$ for simplified notation. G_0 and C_p considered negligible. Outlined section of Mason model in (a) shows parameters lumped into BVD model in (b).

6

TABLE II
SUMMARY OF ANALYTICAL EQUIVALENT CIRCUIT PARAMETERS

Parameter	General: N electrodes Electrode k, mode $(0,n)$	mode $(0,1)$	Single Electrode e Approximation
C_0	$\frac{\epsilon_{33}^{\sigma}\pi(a''^2_k - a'^2_k)}{h_p}\left(1 - k_{31}^2\right)$	$\frac{\epsilon_{33}^{\sigma}\pi a_e^2}{h_p}\left(1 - k_{31}^2\right)$	
N	$\left[\frac{\pi\lambda_{0n}}{2J_1(\lambda_{0n})}\right]e_{31,f}Z_p$	$19.127 e_{31,f}Z_p$	
$K_m = \frac{1}{C_m}$	$\left[\frac{\lambda_{0n}^4}{2}\left(\frac{\lambda_{0n}J_0(\lambda_{0n})}{2J_1(\lambda_{0n})}\right)^2\right]\frac{\pi D}{a^2}$	$197.526\frac{\pi D}{a^2}$	$192\frac{\pi D}{a^2}$ [32]
L_m	$\frac{1}{2}\left(\frac{\lambda_{0n}J_0(\lambda_{0n})}{2J_1(\lambda_{0n})}\right)^2\pi a^2 I_0$	$1.891\pi a^2 I_0$	$\frac{9}{5}\pi a^2 I_0$ [32]
L_r	$\frac{\rho c\pi a^2}{\omega}(ka)\int_k^{\infty}K_n(\mu a)J_1(\mu a)\frac{d\mu}{\sqrt{k^2-\mu^2}}$		$ka < 1: \rho c\pi a^2\frac{ka}{\omega}$
R_r	$\rho c\pi a^2(ka)\int_0^k K_n(\mu a)J_1(\mu a)\frac{d\mu}{\sqrt{k^2-\mu^2}}$		$ka < 1: \rho c\pi a^2\frac{(ka)^2}{2}$
R_m			air: $R_r\times(MLR+1)$ oil: $R_r >> R_m, R_m \approx 0$

The significance of electrode size optimization follows from an electromechanical viewpoint as the coupling factor B_{nk} directly affects the transformation between the electrical and mechanical domain. For appropriate pMUT design, electrodes should be patterned to maintain B_{nk} close to 1 otherwise a reduction in the transformation factor will result in decreased electromechanical transformation leading to reduced sensitivity.

For convenience, Table II summarizes the findings of the following sections, and presents relevant approximations from literature [32] and limiting cases based on physical system parameters and non-dimensionalized constants.

A. Electric Current and k_{31}^2

In the transmit case, when a plate is excited by a sinusoidal external voltage, the electric field results in an electrically induced bending moment applied about the conventionally defined neutral plane z_N (see Appendix A). Therefore in transmit conditions, the electrical neutral plane z_e must be defined as the plane where zero bending moment is present in conditions with an externally applied electric field and is related to the conventionally defined neutral axis z_N via [34]:

$$z_e = z_N - \left(\frac{h_p^2}{12Z_p} + Z_p\right) \tag{9}$$

where the neutral plane with applied electric field Z_e is determined from the distance between the z_N and the center of the piezoelectric layer:

$$Z_e = -\left(\frac{h_p^2}{12Z_p} + Z_p\right) \tag{10}$$

Z_p is length of the moment arm determined by the distance between the z_N and the center of the piezoelectric layer $z_p - h_p/2$:

$$Z_p = z_p - \frac{h_p}{2} - z_N \tag{11}$$

In the piezoelectric layer, the out of plane electrical displacement D_3 is determined by the dielectric constant measured at constant stress ϵ_{33}^{σ} and electric field $E_3 = V/h_p$ both in the z direction, and the in-plane plate strains $\varepsilon_{rr,p}$ and $\varepsilon_{\theta\theta,p}$ that generate charge via 31 mode actuation:

$$D_3 = e_{31,f}\left(\varepsilon_{rr,p} + \varepsilon_{\theta\theta,p}\right) + \frac{\epsilon_{33}^{\sigma}V}{h_p} \tag{12}$$

Further input of the plate strain equations from [28] yields:

$$D_3 = e_{31,f}\left(Z_p - Z_e\right)\left(\frac{1}{r}\frac{\partial W}{\partial r} + \frac{\partial^2 W}{\partial r^2}\right) + \frac{\epsilon_{33}^{\sigma}V}{h_p} \tag{13}$$

7

Electrical current is generated via the bending moment induced by the moment arm between the electrical neutral axis and center of the piezoelectric layer. In [34], it is demonstrated that:

$$e_{31,f} Z_e \left(\frac{1}{r} \frac{\partial W}{\partial r} + \frac{\partial^2 W}{\partial r^2} \right) = \frac{2 d_{31}^2 Y_p V}{h_p (1 - \nu_p)} \tag{14}$$

enabling the separation of the electrical displacement into voltage and deflection dependent components:

$$D_3 = e_{31,f} Z_p \left(\frac{1}{r} \frac{\partial W}{\partial r} + \frac{\partial^2 W}{\partial r^2} \right) + \left(\frac{-2 d_{31}^2 Y_p}{h_p (1 - \nu_p)} + \frac{\epsilon_{33}^\sigma}{h_p} \right) V \tag{15}$$

By definition, the electrical current I_3 is the time dependent derivative of the electrical displacement integrated over the plate area:

$$I_3 = j\omega \int_0^{2\pi} \int_0^a D_3(r) \, r \, dr \, d\theta \tag{16}$$

which in reduced, electrode dependent form becomes [34]:

$$I_{nk} = j\omega \left(2\pi e_{31,f} Z_p \left[r \frac{\partial W_{nk}}{\partial r} \right]_{r=a_k'}^{a_k''} + C_{0,k} V_k \right) \tag{17}$$

where by definition [30] the clamped capacitance C_0 is:

$$C_{0,k} = \left(1 - k_{31}^2 \right) C_{f,k} \tag{18}$$

and the free capacitance C_f is given by:

$$C_{f,k} = \frac{\epsilon_{33}^\sigma \pi \left(a_k''^2 - a_k'^2 \right)}{h_p} \tag{19}$$

with coupling coefficient k_{31}^2:

$$k_{31}^2 = \frac{2 d_{31}^2 Y_p}{\epsilon_{33}^\sigma (1 - \nu_p)} \tag{20}$$

Consistent with other piezoelectric transducer systems [30], the derived coupling coefficient is equivalent to the material planar coupling coefficient for thin film piezoelectric layer in 31 mode. For piezoelectric transducer operation in 31 mode, the limiting value of the effective coupling is determined by the PZT material coupling $k_{31}^2 \approx 20\%$ [35].

B. Mechanical Impedance

The solutions for current and deflection with dependency on applied pressure and voltage form the fundamental building blocks for the governing transduction equations and equivalent circuit representation. For consistency with common mechanical domain modeling, the field and flow variables of force F and velocity u are selected. Since the plate deflection varies across the surface, a velocity must be chosen that will effectively characterize the plate motion. Based on common approaches in transduction literature [30], the average velocity computed over the entire plate surface is selected to characterize the deflection behavior. The average velocity is given as:

$$u_{nk} = \frac{j\omega}{\pi a^2} \int_0^{2\pi} \int_0^a W_{nk}(r) \, r \, dr \tag{21}$$

with simplification:

$$u_{nk} = j\omega \left[\frac{2\pi}{D \Lambda_{0n} (\gamma_{0n}^4 - \gamma^4)} \left[e_{31,f} Z_p \left(\frac{2 J_1(\lambda_{0n})}{\pi \lambda_{0n}} \right) B_{nk} V_k + \left(\frac{2 J_1(\lambda_{0n})}{\pi \lambda_{0n}} \right)^2 P_\omega \right] \right] \tag{22}$$

Similarly, the force is the pressure integrated over the plate area. Assuming the pressure force is constant over the plate surface, the force is simply:

$$F = \pi a^2 P_\omega \tag{23}$$

8

By using an approach similar to [33], admittance values are determined from Equations 7 and 17. Beginning with the electrical portion of the admittance matrix, expansion of Equation 17 by substitution using Equation 7 yields:

$$I_{nk} = j\omega \left[2\pi e_{31,f} Z_p \left(\frac{B_{nk}}{D\Lambda_{0n} \left(\gamma_{0n}^4 - \gamma^4 \right)} \right) \left(e_{31,f} Z_p B_{nk} V_k + \frac{2J_1 \left(\lambda_{0n} \right)}{\pi \lambda_{0n}} P_\omega \right) + C_{0,k} V_k \right] \tag{24}$$

From the governing equations for transducers, the electrical portion of the admittance is known to take the form [33]:

$$\frac{\partial I_{nk}}{\partial V_k} = j\omega C_{0,k} + \frac{\partial I_{nk}}{\partial F} N_n B_{nk} \tag{25}$$

Differentiating Equation 24 with respect to V_k and fitting it to the form of Equation 25 yields:

$$\frac{\partial I_{nk}}{\partial F} = j\omega \left[2\pi e_{31,f} Z_p \left(\frac{B_{nk}}{D\Lambda_{0n} \left(\gamma_{0n}^4 - \gamma^4 \right)} \right) \left(\frac{2J_1 \left(\lambda_{0n} \right)}{\pi \lambda_{0n}} \right) \right] \tag{26}$$

and mode dependent transformation ratio N_n:

$$N_n = \left[\frac{\pi \lambda_{0n}}{2J_1 \left(\lambda_{0n} \right)} \right] e_{31,f} Z_p \tag{27}$$

For piezoelectric transducers, transduction is linear and reciprocal; therefore, reciprocity must be satisfied with the chosen field and flow variables:

$$\frac{\partial I_{nk}}{\partial F} = \frac{\partial u_{nk}}{\partial V_k} \tag{28}$$

As a reciprocity check, differentiation of Equation 22 with respect to V_k yields:

$$\frac{\partial u_{nk}}{\partial V_k} = j\omega \left[2\pi e_{31,f} Z_p \left(\frac{B_{nk}}{D\Lambda_{0n} \left(\gamma_{0n}^4 - \gamma^4 \right)} \right) \left(\frac{2J_1 \left(\lambda_{0n} \right)}{\pi \lambda_{0n}} \right) \right] \tag{29}$$

which is equivalent to $\frac{\partial I_{nk}}{\partial F}$ in Equation 26.

The mechanical impedance is then determined through substitution of Equation 72 for Λ_{0n} and Equation 2 for γ:

$$z_{m,n} = \frac{\partial F}{\partial u_{nk}} = \left(\frac{D\gamma_{0n}^4}{j\omega} + j\omega I_0 \right) \left[\frac{1}{2\pi} \left(\frac{\gamma_{0n} J_0 \left(\lambda_{0n} \right)}{2J_1 \left(\lambda_{0n} \right)} \right)^2 \right] \tag{30}$$

where the first and second terms represent stiffness $K_{m,n}$ and mass $L_{m,n}$ contributions, respectively.

Final modification and simplification of the lumped parameters yields each component in symbolic form:

$$K_{m,n} = b_n \frac{\lambda_{0n}^4 \pi D}{a^2} \tag{31}$$

$$L_{m,n} = b_n \pi a^2 I_0 \tag{32}$$

where b_n is:

$$b_n = \left[\frac{1}{2} \left(\frac{\lambda_{0n} J_0 \left(\lambda_{0n} \right)}{2J_1 \left(\lambda_{0n} \right)} \right)^2 \right] \tag{33}$$

Conveniently, the bracketed term in Equation 27 and b_{0n} are constants determined by the boundary condition mode shape constant λ_{0n} and derived from the characteristic shape profile solution. Therefore, for any clamp plate 31 mode piezoelectric transducer, the constant values will not change and the above equations are valid for equivalent circuit representation.

Using the characteristic variables for electromechanical systems system, the piezoelectric governing transduction equations can now be given as [30]:

$$\begin{aligned} F &= z_{m,n} u_{nk} - N_n B_{nk} V_k \\ I_{nk} &= N_n B_{nk} u_{nk} + Y_{0,k} V_k \end{aligned} \tag{34}$$

where the purely electrical component of the electrical admittance is $Y_{0,k} = j\omega C_{0,k}$.

With the evaluation of constants at the first axisymmetric vibration mode, Equations 27,31, and 32 are written:

$$N_1 \cong 19.127 \frac{Y_p d_{31} Z_p}{1 - \nu_p} \tag{35}$$

$$K_{m,1} \cong 197.526 \frac{\pi D}{a^2} \tag{36}$$

$$L_{m,1} \cong 1.891 \pi a^2 I_0 \tag{37}$$

Previously, Mason employed a similar approach to determine mechanical impedance of a vibrating plate [32]. Although Mason's approach is derived for a single material plate, generalization of the governing plate vibration equation through the lumping mechanical terms into flexural rigidity and surface density allows for comparison between Mason's approach and the current model. For low frequency values, Mason used a power series expansion of the Bessel functions to approximate the stiffness and mass yielding:

$$K_{m,Mason} \approx 192 \frac{\pi D}{a^2} \tag{38}$$

$$L_{m,Mason} \approx \frac{9}{5} \pi a^2 I_0 \tag{39}$$

Mason's approximate mass and stiffness in Equations 31 and 32 are in good agreement with the first mode derived equations.

The electical and mechanical circuit parameters have now been fully defined with proven transduction reciprocity. Further construction of the equivalent circuit requires a shift in focus to acoustic domain modeling, which requires a separate solution technique. As a result, the acoustic domain model is independent of the electromechanical transduction scheme and thus acoustic models are applicable to any clamped, vibrating circular plate system.

C. Acoustic Radiation Impedance

Applying the solution technique derived by Morse and Ingard [31], the vibrating diaphragm is placed along the surface of the infinitely rigid baffle centered at the origin as shown in Figure 6. The pressure at a distance R from the diaphragm center is determined by integrating the pressure gradient source strength and Green's function for infinite baffle wave propagation [31]:

$$P_\omega (r, \phi, z) = j\rho c k \int \int u_\omega (x_0, y_0) G_\omega (r, \phi, z | r_0, \phi_0, 0) \, dx_0 dy_0 \tag{40}$$

where the Green's function for the axisymmetric case in cylindrical coordinates is given by:

$$G_\omega (r, \phi, z | r_0, \phi_0, 0) = \frac{j}{2\pi} \int J_0 (\mu r) J_0 (\mu r_0) \frac{\mu d\mu}{\sqrt{k^2 - \mu^2}} \tag{41}$$

with [31]:

$$\mu = k \sin \theta \tag{42}$$

For a clamped plate with radius a, the deflection is determined by an amplitude constant related to the vibration mode A_{0n} and the characteristic shape profile $\Psi_{0n} (r_0)$ from Equation 4:

$$W (r_0) = \sum_n A_{0n} \Psi_{0n} (r_0) \tag{43}$$

Substituting Equation 41 into 40 and re-writing in cylindrical coordinates yields the finalized form of the pressure integral:

$$P_{\omega,n} (r) = j\omega \rho c k a^2 A_{0n} \int_0^\infty J_0 (\mu r) g_{0n} (\mu a) \frac{\mu d\mu}{\sqrt{k^2 - \mu^2}} \tag{44}$$
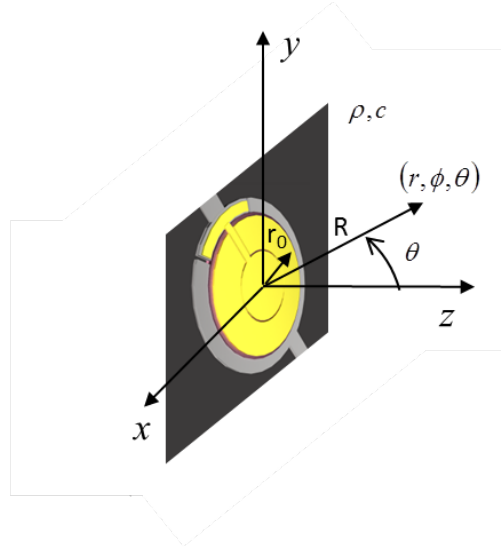
Fig. 6. Coordinate system for diaphragm in an infinite rigid baffle. r_0 denotes coordinates pertaining to the pressure source and r represents coordinates for measured pressure.

where the inner integral $g_{0n}(\mu a)$ is:

$$g_{0n}(\mu a) = \frac{1}{(\mu a)^2 - \lambda_{0n}^2}\left(\mu a J_1(\mu a) J_0(\lambda_{0n}) - \lambda_{0n} J_1(\lambda_{0n}) J_0(\mu a)\right)$$
$$-\frac{J_0(\lambda_{0n})}{I_0(\lambda_{0n})}\frac{1}{(\mu a)^2 + \lambda_{0n}^2}\left(\lambda_{0n} I_1(\lambda_{0n}) J_0(\mu a) + \mu a I_0(\lambda_{0n}) J_1(\mu a)\right) \tag{45}$$

In the pressure integral expression, $g_{0n}(\mu a)$ is the zeroth order Hankel transform of the shape profile function $\Psi(r_0)$. Generally, the zeroth order Hankel transform represents the two-dimensional Fourier-Bessel tranform in polar coordinates. Therefore, $g_{0n}(\mu a)$ and shape profile function $\Psi(r_0)$ form Hankel transform pairs - the cylindrical two-dimensional analog of the Fourier transform pairs.

Since the pressure loading varies in the near field, integration of Equation 44 over the diaphragm surface area is necessary to determine the overall force:

$$F_n = 2\pi \int_0^a P_{\omega,n}(r) r\,dr = j\omega 2\pi\rho c k a^3 A_{0n} \int_0^{k+j\infty} g_{0n}(\mu a) J_1(\mu a) \frac{d\mu}{\sqrt{k^2 - \mu^2}} \tag{46}$$

From the pressure force and with substitution of Equation 43 into Equation 21, the radiation impedance is determined with the average velocity as the flow variable:

$$Z_{r,n} = \frac{F_n}{\langle u_{nk}\rangle} = \pi a^2 \rho c (ka) \frac{\lambda_{0n}}{2J_1(\lambda_{0n})}\left[\int_0^k g_{0n}(\mu a) J_1(\mu a) \frac{d\mu}{\sqrt{k^2 - \mu^2}}\right.$$
$$\left. +j\int_k^\infty g_{0n}(\mu a) J_1(\mu a) \frac{d\mu}{\sqrt{k^2 - \mu^2}}\right] \tag{47}$$

where dimensionless resistance $r_{r,n}$ and reactance $x_{r,n}$ terms are extracted as:

$$Z_{r,n} = \pi a^2 \rho c (r_{r,n} + jx_{r,n}) \tag{48}$$

For the lumped parameter model, the resistive and inductive acoustic terms are further defined as:

$$R_{r,n} = \pi a^2 \rho c r_{r,n} \tag{49}$$

11

and

$$L_{r,n} = \pi a^2 \rho c \frac{x_{r,n}}{\omega} \tag{50}$$

The integral in Equation 47 is difficult to solve analytically, so a numerical integration using the integral function in Matlab is used to generate the solution curves in Figure 7 and discrete values in Table III. A similar integral, that for the rigid piston model provided in [31], was computed using the same integral function and compared with the available analytical solution to confirm function accuracy.

Since the physical system is similar and the solution approach is the same in both cases, the impedance in the rigid piston and plate vibration models should behave similarly with differences attributed to the variation in velocity across the plate surface. The validity of the plate vibration model is assessed drawing comparison to the rigid piston case and through understanding of the limiting cases of the physical system. In the $ka >> 1$ regime, the wavelength $\lambda << 2\pi a$ is small compared to the size of the device and the radiation impedance becomes almost purely resistive and equivalent to the area multiplied by the characteristic acoustic impedance of the medium or $\rho c \pi a^2$ [31].

In the opposite case for $ka << 1$ when the wavelength is long compared to size, the mean outflow from the transducer is approximately uniform, behaving like a point source. Here, the radiation resistance varies from the reactance by a factor of ka; thus, the reactive component dominates. Particularly for small ka, the resistive and reactive loading is nearly the same in both cases. As such, it should be valid to apply the same approximations for $ka < 1$ from the rigid piston case to the plate vibration approach. From [36], the dimensionless radiation resistance can be approximated as:

$$r_r \approx (ka)^2 / 2 \tag{51}$$

and likewise dimensionless reactance becomes:

$$x_r \approx ka \tag{52}$$

As expected, the approximations shows strong agreement with the analytical values for $ka < 1$ in Figure 7. In general for both the rigid piston and plate vibration cases, the high and low ka limiting behaviors are observable.
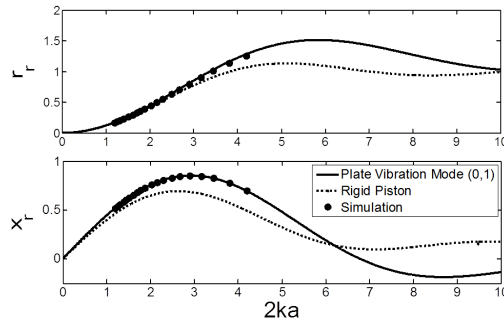

Fig. 7. Dimensionless resistance r_r and reactance x_r components of the radiation impedance for the rigid piston model and the current plate vibration derivation near the first axisymmetric vibration mode. Values provided for specific values of ka shown in Table III. Simplified r_r and x_r given by Equations 51 and 52, respectively provide valid approximation for small ka.

D. Directivity

With the definition of μ in Equation 42, the angular dependence is already implicitly considered in the acoustic impedance derivation and is effectively eliminated through the force integration over the surface of the pMUT. Based on the form of the impedance integral presented in [36] and discussion on the angular dependence of intensity in [31], the directivity can be directly extracted from the above acoustic impedance determination.

By definition, directionality is the ratio of the far field pressure at an angle θ to the on axis far field pressure with $\theta = 0$ [37]. Consistent with assumptions made by Porter [37] and Pritchard [36], radiator directivity at large

TABLE III
DIMENSIONLESS RADIATION IMPEDANCE VALUES

ka	x_r	r_r
0.1	0.0933	0.0050
0.2	0.1855	0.0199
0.3	0.2753	0.0445
0.4	0.3617	0.0785
0.5	0.4435	0.1213
0.6	0.5200	0.1723
0.7	0.5900	0.2308
0.8	0.6529	0.2960
0.9	0.7080	0.3668
1	0.7547	0.4424
1.5	0.8530	0.8532
2	0.7381	1.2233
2.5	0.4818	1.4538
3	0.1907	1.5106
3.5	-0.0405	1.4262
4	-0.1628	1.2728
4.5	-0.1805	1.1246
5	-0.1341	1.0280
5.5	-0.0726	0.9915
6	-0.0297	0.9954

distances from the surface $K = K(\mu, \phi)$ is independent of the radial coordinate r:

$$K(\mu, \phi) = \frac{P_\omega(\mu, \phi)}{P_\omega(\mu = 0, \phi)} = \frac{\int u_\omega(r_0, \phi) J_0(\mu r_0) \mu r_0 dr_0}{\int u_\omega(r_0, \phi) r_0 dr_0} \quad (53)$$

where the pressure is calculated using Equation 44. Finally from the directivity, an alternative form of radiation impedance in Equation 47 based on that given by [36] can be written:

$$Z_{r,n} = \rho c \pi a^2 (ka) \int_0^{k+j\infty} K_n(\mu a) J_1(\mu a) \frac{d\mu}{\sqrt{k^2 - \mu^2}} \quad (54)$$

As a check of the directivity calculation, a constant velocity represents the rigid piston case, which when input into Equation 53 yields the well-established beam pattern for rigid piston radiation [31]:

$$K_{rp}(\mu a) = \frac{2 J_0(\mu a)}{\mu a} \quad (55)$$

as shown in Figure 8. Using the previous calculated integrals in Equations 45 and 21 and the directivity definition in Equation 53 yields the axisymmetric mode dependent directivity of the vibrating plate:

$$K_n(\mu a) = \frac{\lambda_{0n} g_{0n}(\mu a)}{2 J_1(\lambda_{0n})} \quad (56)$$

For validation of the determined directivity, the beam pattern intensity with reference to its maximum value at a measurement point perpendicular to the surface is shown plotted against the dimensionless variable $\mu a = ka \sin\theta$ in Figure 8. It is significant to note that this pattern holds for any value of ka, and the directivity intensity is bounded by the minimum values set by $|ka|$. Simulated values specific to a single pMUT near its fundamental resonance in a vegetable oil environment show strong agreement with the derived directivity $K(\mu)$. Comparison with the rigid piston model shows deviation between the piston and plate increases with ka.

Based on typical length scales and fluid properties for a micro-scale ultrasonic transducer used in medical applications, a single device operated in an oil medium is generally bounded by $0.1 < ka < 1$, justifying the bounding points represented at the top of Figure 8. Here the wavelength is small compared to the size of the device, but not negligibly small. As such, wave propagation occurs with nearly uniform radial intensity from the
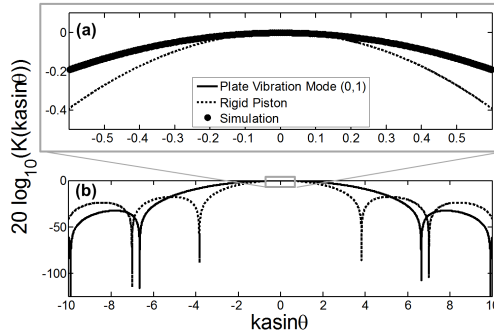
13

Fig. 8. Beam pattern as a function of the dimensionless variable $kasin\theta = \mu a$. Inset (a) shows range of common ka values for MUTs used in medical ultrasound with comparison to a simulated pMUT near fundamental resonance. Model and simulation curves difficult to discern because of good agreement. Analytical model compared to rigid piston model for larger μa in (b). Minima represent grating lobes present for higher values of ka.

MUT similar to that from a point source. However, intensity loss proportional to ka occurs off the axis of maximum response and is observable in the directivity shown in Figure 8.

IV. FABRICATION

For substantive model verification, a single electrode pMUT cell design with varying electrode size is selected. Given the relation between electrode size and transformation coupling through B_{11}, electrode size is expected to have an easily measurable influence on electrical parameters. Since electrode size is simply modified through lithographic patterning, validation of the model can be made on the substrate level ensuring consistency in the material properties and piezoelectric film quality between tested devices. Various plate radii were also patterned to achieve varying resonant frequencies, with larger lower frequency ($< 1MHz$) devices representing NDT and range finding applications and smaller, higher frequency devices ($> 1MHz$) considered for medical ultrasound.

The pMUT fabrication process starts with a Silicon-on-Insulator (SOI) wafer consisting of $3.5\mu m$ silicon device and $1\mu m$ buried silicon oxide layers. Thermal oxide is grown on the wafer and image reversal photolithography is used to pattern the bottom electrode and electrical routing to contact pads on the edge of chips. Electron beam deposition of $30nm/200nm$ of Ti/Pt forms the bottom electrode layer followed by lift-off to achieved the final patterning.

Next, a multi-layer $Pb\left(Zr_{0.52}\right)Ti_{0.48}O_3$ film is deposited, patterned and annealed on the substrate. 15 wt% PZT sol-gel (PZT $52/48$ solution E1 purchased from Mitsubishi Materials) is spin coated onto the substrate and then pyrolyzed at $350°C$. Subsequent layers are deposited following the same approach. After pyrolysis, PZT is patterned via standard photolithography and etched with a quick exposure to a $20:6:1$ mixture of DI water: hydrochloric acid: buffered oxide etch immediately followed by vigorous rinsing in DI water. Once the photoresist is removed, the PZT is annealed in a furnace at $700°C$ with oxygen flow.

The top electrode is patterned using the same image reversal photolithography and lift-off technique except with electron beam deposition of $30nm/175nm$ of Ti/Au. In addition to patterning of the top electrode, Au is deposited on the contact pads at the chip edge for wire bonding. Finally, the diaphragm and chips are released with a Deep Reactive Ion Etching (DRIE) of the handle wafer from the back side using the buried oxide as an etch stop. The fabrication process flow is shown in Figure 9, and measured thicknesses of tested pMUT devices are shown in Table I.

Scanning electron microscope (SEM) images of the final device cross-sections are shown in Figure 10. Over-etching is observed as part of the common 'footing' defect that results from charge build-up on the buried oxide layer of the SOI substrate during DRIE. Steps were taken to minimize the footing effects by modifying handle wafer thickness, etch time, chamber pressure and other parameters. However, for model confirmation, the diaphragm radius is adjusted based on the SEM cross-sectional images to reflect over-etching. As a general rule, over-etching is aspect ratio dependent and therefore increases with device radius. For the large devices, over-etching of $\approx 40\%$ is observed, which is consistent the cross-section shown in Figure 10.
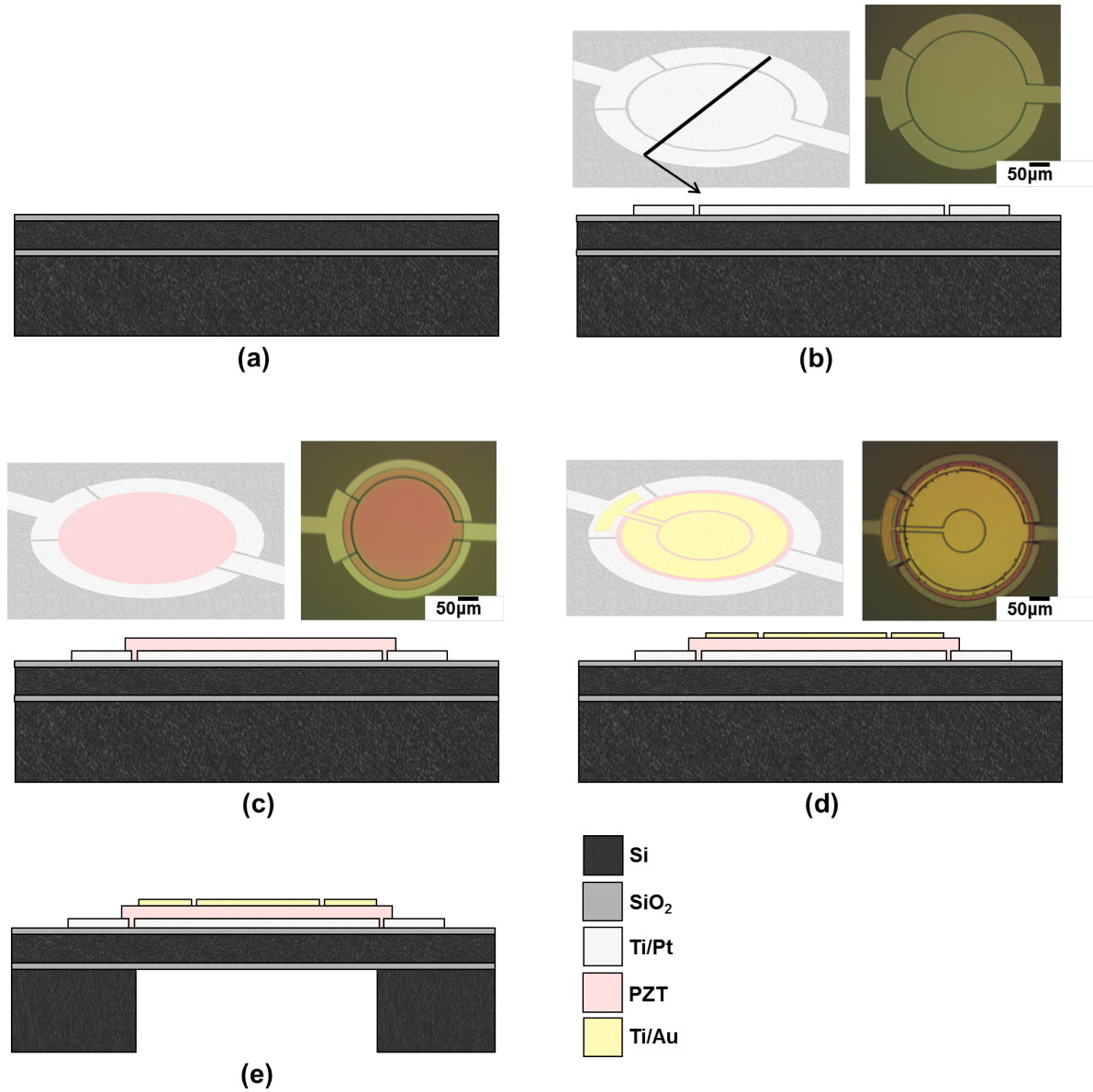
14

Fig. 9. pMUT fabrication process flow with cross-section images of the SOI substrate after thermal oxide growth (a), bottom electrode deposition (b), PZT deposition and etching (c), top electrode deposition (d), and back side DRIE (e). Rendered isometric view (left) and microscope (right) images of the devices during processing shown in (b), (c), and (d).

V. EXPERIMENT

A. Dynamic Deflection

The resonant frequency of pMUT cells are measured using a laser doppler vibrometer (LDV, Model MSA-500 Micro System Analyzer with extended frequency range capability, courtesy of Polytec, Inc.) via a frequency sweep with 1V excitation. Results are shown in Figure 11a for pMUTs with radii similar to devices used in subsequent electrical and static deflection tests.

For the first three axisymmetric vibration modes, the measured deflection profile is normalized and compared to the dimensionless shape profile from Equation 4 in Figure 11b-d. For $n = 1, 2, 3$, the constant $\lambda_{0n} = 3.197, 6.307, 9.44$
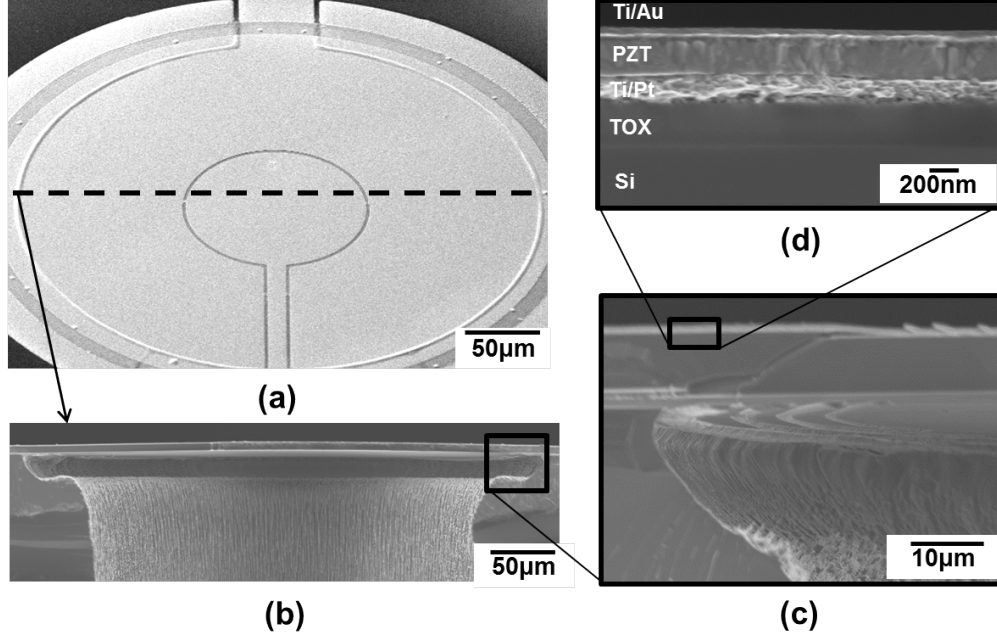
Fig. 10. SEM of finished pMUT device with top view (a) and cross sections in (b-d). Over-etch defect shown in greater detail in (c) and labeled top layer view in (d).

which is taken from plate vibration literature [31]. Strong agreement between the measured profile and model indicate that the diaphragms are vibrating within the plate regime, and the influence of tension from residual stresses is assumed to be minimal, which is neglected in the current analysis.

From SEM images such as those in Figure 10, the fundamental resonant frequency is calculated according to Equation 6 by inputting the etched plate radius, layer thicknesses and material properties. Strong agreement between the model and measured resonant frequency demonstrates both the validity of Equation 6 [31] and confirms the calculation of D, I_0, and a for further use in the equivalent circuit model.

B. Static Deflection and $e_{31,f}$ Measurement

With the proven dominance of plate mode bending, the deflection model is applied to the static bending case using Equation 7 neglecting pressure. Previously, the static model was compared to both experimental data and an alternative energy based deflection derivation demonstrating strong agreement [28]. With the validated model, static deflection is now used to directly determine the piezoelectric constant $e_{31,f}$, which bypasses the specialized wafer flexure set-up typically required for the 31 piezoelectric constant measurement [38]. Static deflection is measured over a range of applied bias voltages using an optical profilometer (ZYGO Corp.). Differential deflection averaged over the electrode area is compared to the $0V$ reference state. For the single electrode case only considering the first vibration mode, the deflection scales with bias voltage as:

$$W_{avg,11} = \frac{e_{31,f}Z_p}{D\Lambda_{01}\gamma_{01}^4} B_{11}V_{DC} \left[\frac{1}{\pi a_e^2} \int_0^{2\pi} \int_0^{a_e} \Psi\left(r_0\right) r_0 dr_0 d\theta_0 \right] = -MV_{DC} \tag{57}$$

where the slope M becomes:

$$M = \frac{2e_{31,f}Z_p}{D\Lambda_{01}\gamma_{01}^4} \left[J_1\left(\gamma_{01}a_e\right)^2 - \left(\frac{J_0\left(\lambda_{01}\right)}{I_0\left(\lambda_{01}\right)}I_1\left(\gamma_{01}a_e\right)\right)^2 \right] \tag{58}$$

From the resonant frequency, the etched radius is determined using the approach described in the previous section. All other geometric parameters and constants that define the slope M are known. For devices characterized in Table
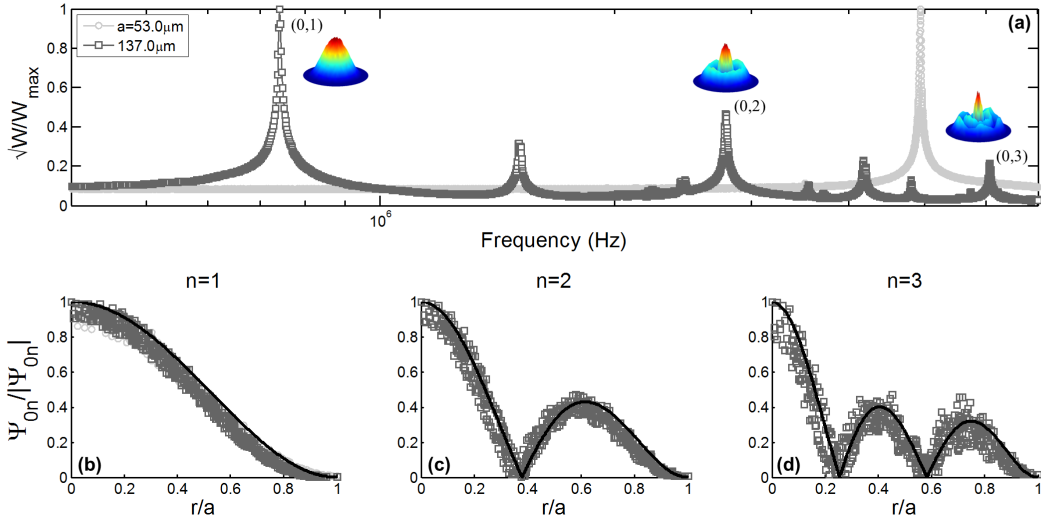
16

Fig. 11. LDV frequency sweep measurement normalized to deflection at fundamental resonant mode (a), insets show 3D views of raw profile data (axes not to scale) for $a = 137.0\mu m$ device at each axisymmetric mode. Normalized profile slices as a function of dimensionless radius compared to shape profile in Equation 4 for $n = 1, 2, 3$ axisymmetric vibration modes shown in (b)-(d), respectively.
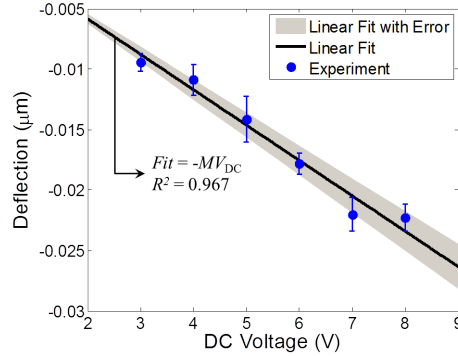

Fig. 12. Differential deflection averaged over the center electrode area measured from four separate devices with the same geometry. Slope extracted from linear fit through the origin with robustness demonstrated via high R^2. Standard error shows the consistency of measurement with $e_{31,f} = -8.56 \pm 0.6 C/m^2$ calculated using Equation 58.

IV, $e_{31,f} = -8.56 \pm 0.6 C/m^2$ is determined from a linear fit of the deflection vs. bias voltage data and Equation 58 and is consistent with typical values for thin film $Pb\left(Zr_{0.52}\right)Ti_{0.48}O_3$ [35].

Electrode size dependence is determined in a similar manner using the linear fit of differential deflection and bias voltage. Since the electrode size varies, the slope is adjusted to account for the varying area used in the deflection profile average. Experimental data is plotted as $M/\Psi_{avg,11}$ in Figure 3 where $\Psi_{avg,11}$ is represented by the bracketed term in Equation 57. All data is normalized to the maximum value of $M/\Psi_{avg,1}$ achieved at $a_e/a = 0.64$ with error bars showing standard error. Measurements were performed on devices with $a = 139.5 \pm 0.2\mu m$ and layer thicknesses shown in Table I. Extracted $e_{31,f} = -6.35 \pm 1.06 C/m^2$ is again consistent with common values [35] and demonstrates the typical variation in deposited sol-gel PZT quality across wafer substrates.

C. Electrical Impedance

Transduction performance is further evaluated using electrical impedance measurements (Model 1260A Impedance/Gain-phase Analyzer, Solartron Inc.) with a frequency sweep with $V_1 = 1V$ near the fundamental
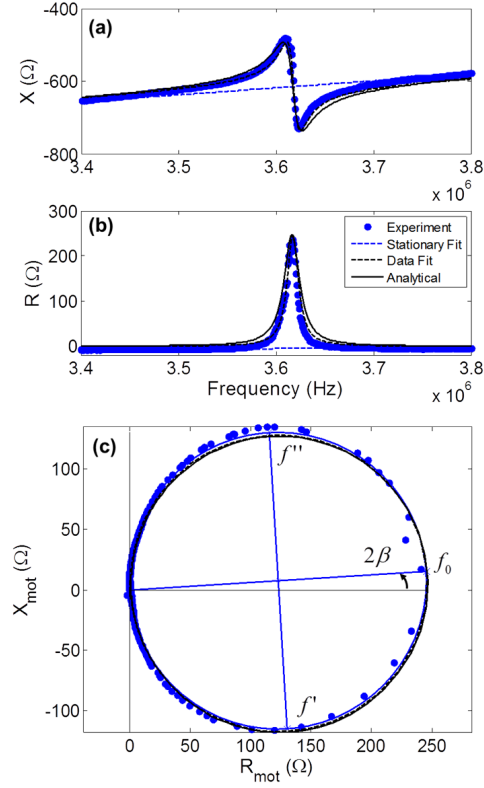
Fig. 13. Imaginary X (a) and Real R (b) components of the experimentally measured electrical impedance showing linear interpolation for stationary data fit. Motional impedance loop with circle fit (c) showing center resonant frequency f_0, half power frequencies f' and f'', and angle 2β. Motional impedance results when stationary fit subtracted from total impedance. Parameter values for this device and neighboring devices reported in Table IV.

resonant mode. Impedance measurements are calibrated using a standard open/short compensation technique to remove the effects of the measurement probes and cables. Typically, a form of least square curve fitting is then employed to calculated the lumped parameters of the BVD model directly from the impedance data. However, it is found that this method is very sensitive to initial conditions and is difficult to implement when the anticipated values of lumped parameters vary by many orders of magnitude. Given this limitation, an iterative fitting technique, based on experimentally extracted values and known transduction metrics for piezoelectric transducer systems, is developed for higher accuracy and less sensitive fitting, as it does not require guessing initial conditions.

1) Stationary Components: The iterative fitting process begins by separating static and motional impedance following a classical approach to impedance data fitting provided by [39]. A linear interpolation of the imaginary and real raw data at frequencies above and below the resonant and anti-resonant peaks is used to determine the static electrical reactive X_e and resistive R_e terms, respectively, which are then subtracted from the total imaginary and real impedances to determine motional impedance components. Sample experimental data with stationary fitting is shown in Figure 13.

From the linear fit, the shunt capacitance defined in Equation 18 is directly determined by the static reactance according to:

$$C_0 = \frac{-1}{\omega X_e} = \frac{\epsilon_{33}^{\sigma} \pi a_e^2}{h_p} \left(1 - k_{31}^2\right) \tag{59}$$

Like many perovskite phase ferroelectric materials, PZT has a high dielectric constant, which results in a shunt capacitance larger than anticipated parasitics. However, for highest accuracy, impedance measurements were made via direct device probing to remove parasitic effects of electrical routing. For the analytical model and simulation,

18

the relative dielectric constant $\epsilon^{\sigma}_{33}/\epsilon_0 = 800$ is selected, which shows a strong fit with the experimental data in Figure 14a and falls within the range of common values for thin film PZT [40]. The shunt capacitance measurement is validated through comparison to a measured bulk capacitor of similar capacitance.

In experiment, it is found that application of the appropriate DC bias voltage is required to minimize dielectric loss and maximize the piezoelectric constant near resonance. In this way, static conductance G_0 is considered negligible in subsequent calculations, which is consistent with the treatment of conventional piezoelectric transducer systems [30]. The cumulative sum of the required bias field and amplitude of the AC signal is on the order of $3x$ the coercive field of the PZT, which is consistent with fields typically applied for poling [41]. Unlike in the bulk case, for thin film piezoelectric systems, it is common for a biasing DC electric field to be added to an AC field to maintain polarization when the operating AC field is close to the coercive field [35]. Biasing is also found to reduce the loss tangent in piezoelectric thin films [29], [42]. Despite the application of bias voltage, $e_{31,f}$ extracted from the best fit circuit parameters and confirmed with simulations is smaller than in the static case as shown in Table IV.

2) Motional Components: Motional lumped parameters are determined from lumped parameter based definitions of metrics measured directly from experiment. In experiment, the sharpness of the resonant peak, referred to as the mechanical quality factor Q_m is measured and related to lumped parameters by [30].

$$Q_m = \omega_0 \frac{L}{R} = \frac{f_0}{f'' - f'} \tag{60}$$

where $(f'' - f')/f_0$ is the fractional bandwidth at half-power or $-3dB$ fractional bandwidth. Graphically, Q_m is determined following the approach in [39]. After subtraction of stationary components from total impedance, a circular fit of the vector locus of the motional impedance is performed as shown in Figure 13c. From the circle radius and the angle 2β formed between the circle center and origin, the coordinates of the half-power f' and f'' frequencies are geometrically determined and represent the frequencies at which the real and imaginary components of the impedance are equal.

Other metrics used for fitting include the effective electromechanical coupling k^2_{eff} [30]:

$$k^2_{eff} = \frac{N^2 C}{N^2 C + C_0} = 1 - \frac{f_0^2}{f_a^2} \tag{61}$$

measured from the anti-resonant frequency at the local maximum f_a and resonant frequency at the local minimum f_0 of the impedance magnitude data. Finally, the angular resonant frequency $\omega_0 = 2\pi f_0$ is alternatively defined as:

$$\omega_0 = \frac{1}{\sqrt{LC}} \tag{62}$$

The experimentally determined values in Equations 59, 60, 61, and 62 are then input into the iterative fitting model described in Appendix D to determine the best fit lumped parameters.

With fluid medium and mechanical dissipation, the resonant peak is slightly damped widening the apparent gap between the resonant and anti-resonant peak resulting in an artificially high k^2_{eff} measurement as shown in Table IV. Based on this error, it is recommended that the capacitance based definition of k^2_{eff} should be reported over the experimentally determined frequency based definition, both shown in Equation 61. Since the calculated quality factor is less sensitive to the linear interpolation fit as demonstrated in Table IV, the directly measured value of Q_m is generally valid.

VI. IMPEDANCE MODEL VALIDATION

Electrical impedance parameter fitting from pMUTs with varying electrode coverage are collected to support the current circuit modeling endeavor (Figure 14). For best comparison, data for electrode size variation is collected on chips from the same wafer with similar material stack thicknesses. However, across wafer variation in PZT quality and etching resulted in variation of the piezoelectric constants on a chip-by-chip basis. For a more universally accurate data comparison, the modified transformation ratio is introduced to remove the piezoelectric constant dependence:

$$N' = \frac{N}{e_{31,f}} \tag{63}$$

	Parameter	Data Fit(Measured)	Analytical Model $e_{31,f} = -5.5 C/m^2$
General	$a_{exp}(\mu m)$	62.6 ± 0.3	
	a_e/a	0.479 ± 0.002	
	$e_{31,f}$ (C/m^2, static)	-8.56 ± 0.6	
	$e_{31,f}$ (C/m^2, $3-4MHz$)	-5.5 ± 0.15	
	$C_0(pF)$	70.3 ± 0.9	76
	$CN^2(pF)$	0.120 ± 0.007	0.120
	$k_{eff}^2(\%)$	$0.165 \pm 0.009\,(0.734)$	0.171
Air	$f_0(MHz)$	3.554 ± 0.030	
	$L/N^2(mH)$	17.4 ± 0.9	16.7
	$R/N^2(\Omega)$	1481 ± 43	
	MLR	5.1 ± 0.34	
	Q_m	$264.9 \pm 20.2\,(298.7)$	

Data collected from 2D patterned cells on the same chip.

Simulations with varying $e_{31,f}$ values confirm that the definitions of motional parameters based on N' are equivalent, which agrees with the analytical modeling prediction. For mass and capacitance parameters, simulation, analytical model and experimental data show strong agreement (see Figure 14) confirming the accuracy of the Green's function based approaches.

Although the motional resistance trend as a function of electrode radial coverage is similar, the measured resistance is much larger than simulated and analytical values. Since mechanical dissipation is difficult to predict, the mechanical resistance is initially not included in the analytical and simulation model. However, from the data fit to experimental data, the total resistance including the mechanical and acoustic components is extracted. For most MEMS resonator systems, mechanical dissipation is due to thermoelastic losses and is anticipated to be larger than the acoustic loading resistance in air [43]. In the engineering of traditional bulk ultrasonic devices, the mechanical loss ratio MLR relates mechanical resistance R_m to acoustic resistance R_r as:

$$MLR = R_m/R_r \tag{64}$$

and is a common metric for quantifying dissipation [44]. Using this approach, the mechanical dissipation is empirically determined from analytical and measured data with standard error as $MLR = 5.21 \pm 0.27$ for data presented in Figure 14d. As expected, MLR is constant with limited variation for diaphragms of similar geometry. The total motional resistance R can then be estimated as:

$$R = (MLR + 1)\,R_r \tag{65}$$

and shows strong agreement with the experimentally measured values in Figure 14d.

The raw experimental impedance curve data is compared to the analytical model via substitution of the empirically calculated R from Equation 65 into the system transfer function. When both are included in the analytical model, the resulting total and motional impedance data aligns well with the modified analytical model as shown in Figure 13. Transfer functions in Figure 15 plotted with lumped parameters shown in Figure 14. Figure 15 demonstrates efficacy of model and data fit to experiment over a range of electrode sizes.

On-chip pMUT variation is further evaluated through measurement of identical 2D patterned transducer cells. Relevant metrics, extracted parameters, and device geometry in Table IV demonstrate the repeatability of the data fitting and consistency of on-chip device performance.

VII. DISCUSSION

A generalized form of the arbitrary electrode, axisymmetric vibration mode Mason equivalent circuit for a clamped, circular plate pMUT is presented. From the most general form, the electrical, mechanical and acoustic domain lumped parameters are defined for the fundamental vibration mode, single electrode case. With the lumped parameter determinations validated with experiment and simulation, design suggestions can be made based on
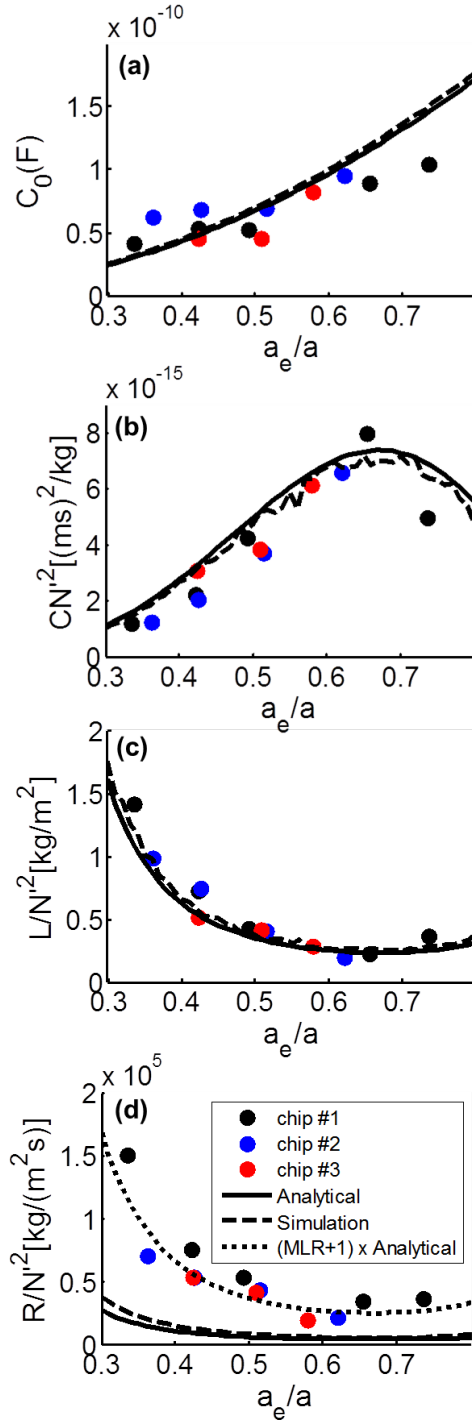
Fig. 14. Shunt capacitance (a), modified motional compliance (b), inductance (c), and resistance (d) as a function of electrode radial coverage where N' is defined in Equation 63. MLR determined empirically from Equation 64 as $MLR = 5.21 \pm 0.27$.
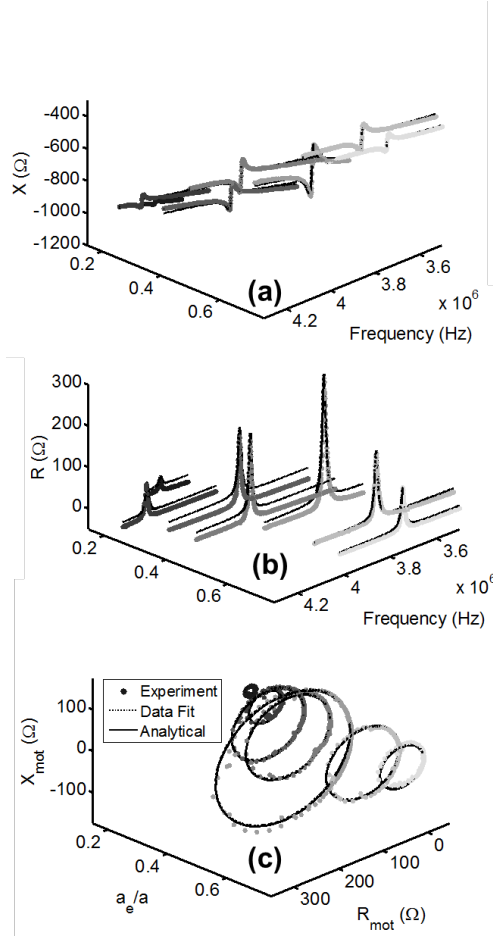
Fig. 15. Experimental data including lumped parameter data fit and analytical model with MLR and measured stationary capacitance as a function of electrode radial coverage. Motional impedance (a) and total imaginary (b) and real (c) impedance as a function of frequency and correspond with extracted parameters for chip #1 in Figure 14. Close fit demonstrates robustness of fitting technique and strength of analytical model.

structural and material property dependence. The initial design is fabricated with a focus on residual stress reduction through the use of a dummy outer electrode and thick silicon device layer. As a result from the vibration mode shape measurements and static deflection, pMUT vibration is shown to be plate mode and the influence of tension caused by residual stress is negligible. Further work is needed to evaluate the extent of the stress-free model applicability to pMUT designs with smaller relative thickness of supporting structural layers. In these cases, it is strongly suggested that the plate model is only applied when the stiffness is confirmed to dominate deflection and vibration behavior as was demonstrated in the current work. Determination of residual stress effects is the subject of future work, which can be achieved through the addition of a second order residual stress induced tension term in Equation 1 (see [45] for tension modified plate vibration equation) and an analogous solution technique.

However, residual stress reduction comes at a cost: the thick, inactive silicon layer acts to reduce the effective electromechanical coupling. In future design endeavors, thickness and material selection of the active and inactive material layers should be optimized via Equation 61 with achievable performance bounded by fundamental material coupling k_{31}^2. As in MEMS cantilever systems [46], it is realistic to assume that the upper limit of the achievable electromechanical coupling is approximately $k_{31}^2/2$. For increased driving efficiency, the shunt capacitance should be minimized without compromising high transformation N and compliance values C_m, which is most easily achieved with high k_{31}^2. In this way, k_{31}^2 is a critical figure of merit in selection of the appropriate piezoelectric material for any 31 mode MEMS based vibrating plate system. However, k_{31}^2 must balanced with a high force output figure of

merit $e_{31,f}$. Strong transformation between the electrical and mechanical domains defined by N relates directly to pressure output and sensitivity. Since N scales directly with $e_{31,f}$, the ideal piezoelectric material for high effective electromechanical coupling and increased sensitivity must have high k_{31}^2 and $e_{31,f}$ making engineered relaxor ferroelectrics like $PMN - PT$ an attractive selection based on increased piezoelectric response [47]. Although aluminum nitride (AlN) can achieve comparable k_{31}^2 to PZT, lower $e_{31,f}$ makes AlN more suited for applications where sensitivity can be sacrificed for decreased shunt capacitance.

Additional improvement in electromechanical transformation is achieved through DC bias voltage application. Consistent with previous results [29], [42], bias voltage increases $e_{31,f}$ and offset the dielectric loss responsible for static resistance. At high frequency, the application of the bias voltage can minimize the loss tangent and maximize responsiveness; however, a reduction in $e_{31,f}$ compared to the static case is still present and likely caused by de-poling effects. It can be assumed that this reduction is unavoidable and further work is necessary to strongly confirm the relation between static and dynamic $e_{31,f}$. The validated static and dynamic plate vibration models introduced here demonstrate the capability of direct quantification of thin film piezoelectric constant for comparison between static and dynamic cases.

The mechanical, transformation, and electrical domain parameters are similarly defined regardless of the pMUT application. Given the separate derivation approach in the acoustic domain, the acoustic parameters are valid for any vibrating, clamped circular plate system and are therefore applicable to alternative actuation mechanisms including electromagnetic and electrostatic systems, particularly cMUTs. For ultrasonic systems, application is largely dependent on size, frequency, and fluid loading conditions and determination of acoustic parameters must be carefully considered based on the dimensionless acoustic parameter ka at resonance in each of these application.

Generally for medical ultrasound applications, a single cell falls within the $ka < 1$ but in air loading for NDT and range finding, $ka > 1$ is possible. When $ka < 1$, the convenient polynomial approximations for R_r and L_r are valid and the nearly omni-directional directivity mimics that of a point source. With $ka > 1$, limiting approximations for acoustic impedance no longer hold and design should be selected with roughly $ka < 6$ to prevent grating lobes. As a tool to the vibrating plate designer, a table of exact values for non-dimensionalized radiation resistance and reactance is provided based on calculated ka (Table III), and is useful for regimes where limiting case approximations do not apply.

In the mechanical domain, resistance is difficult to directly calculate and the empirically determined MLR is introduced to quantify R_m as a function of R_r. MLR is shown to be independent of electrode size but is likely material thickness and signal dependent, and more work is necessary to further understand the relation. However, a quick comparison of the radiation resistance between oil and air loaded environments provides justification for limiting case approximations. Assuming that MLR does not vary greatly between the oil and air loaded cases and for safe assumption $MLR_{air} \approx \mathcal{O}(10)$, the oil loading case is predicted by:

$$MLR_{oil} = MLR_{air} \frac{(\rho c r_r)_{air}}{(\rho c r_r)_{oil}} \tag{66}$$

Since r_r only varies between approximately 0 and 1 and $(\rho c)_{air} / (\rho c)_{oil} = \mathcal{O}(10^{-4})$, the worst case limits $MLR_{oil} << 1$. In most fluid loading cases representative of a medical ultrasound environment, it is likely safe to assume that R_m is negligible but it might be necessary to check this assumption with empirical data. Particularly, since heat dissipation likely scales with signal amplitude, the small AC signal amplitude ($V_0 = 1V$) used in the current determination of MLR_{air} might underestimate more realistic driving conditions, so care must be taken with the limiting approximation.

Beyond the single electrode system, it is the hope of the authors that the general form of the equivalent circuit can be advantageous for optimization of novel designs that have yet to be considered. For example, in conventional multi-layer bulk transducer systems, wideband transmission performance has been demonstrated by using higher order resonant modes [30]. For increased output, Sammoura et al. [48] proposed a two electrode pMUT design where a center circular electrode and outer ring electrode are excited at voltages of the same magnitude and opposite polarity. Model use is not limited to these representative examples but demonstrate the utility of the general analytical circuit for real and novel applications.

VIII. Conclusions

An analytical model with defined Mason equivalent circuit parameters is enumerated for the general case of the arbitrary electrode, axisymmetric vibration mode, circular clamped plate pMUT cell. Acoustic domain modeling is applicable to any vibrating plate system, which can prove useful in the analysis of both cMUT and pMUT systems. For the single electrode fundamental vibration mode case, fabricated thin film PZT based pMUT cells with various electrode sizes confirm the developed model through electrical impedance measurement, which is further supported with simulation using custom defined thin film PZT material.

The explicit definition of Mason model lumped parameters is based on geometry and material properties enabling straight forward implementation in fields including range finding, non-destructive testing and medical ultrasound. Evaluation of lumped parameters is focused on model validation but is presented in a form amenable to future design optimization. Building on the derived analytical equations, relevant simplifications based on operating regimes defined by geometric and system parameters provides further ease of use in application of the developed lumped parameter models. Finally, the utility of the analytical model is proved through formulation of preliminary suggestions for improved electromechanical performance. This serves as the basis for future work to analytically quantify key performance metrics including bandwidth, transmit and receiving sensitivity, output power, and efficiency based on the derived equivalent circuit.

Appendix A

As before, the unimorph pMUT consists of a stack of a q isotropic material layers with an overall thickness $\sum_{i=1}^{q} h_i$. The height z_i of material layer i referenced from the plate bottom at $z = 0$ is determined by the thickness h of each preceding layer via $z_i = \sum_{j=0}^{i} h_j$. Neglecting electric field contributions and assuming the poisson ratio of each layer ν_i is similar, the multi-layer plate neutral plane z_N is conventionally defined as:

$$z_N = \frac{1}{2} \sum_{i=1}^{q} \frac{\frac{Y_i \left(z_i^2 - z_{i-1}^2 \right)}{1 - \nu_i^2}}{\frac{Y_i h_i}{1 - \nu_i^2}} \tag{67}$$

where Y_i is the Young's Modulus of material layer i [3]. By integrating the plate stress-strain constitutive relations to determine bending moments about the neutral plane, the flexural rigidity D is defined [28]:

$$D = \sum_{i=1}^{q} \frac{Y_i}{3 \left(1 - \nu_i^2 \right)} \left[\left(z_i - z_N \right)^3 - \left(z_{i-1} - z_N \right)^3 \right] \tag{68}$$

and the inertial term is determined from Hamilton's principle where surface density I_0 is [49]:

$$I_0 = \sum_{i=1}^{q} \rho_i h_i \tag{69}$$

Appendix B

For a clamped plate, the deflection solution is determined by the green's function and the right hand side of Equation 1 commonly referred to as the forcing function $f(r)$:

$$W(r_0) = -\int_0^a f(r) G(r|r_0) r \, dr \tag{70}$$

From before [28], the axisymmetric Green's function is defined as:

$$G(r|r_0) = \sum_n \frac{\Psi_{0n}(r) \Psi_{0n}(r_0)}{\Lambda_{0n} \left(\gamma_{0n}^4 - \gamma^4 \right)} \tag{71}$$

with deflection profile constant Λ_{0n}:

$$\Lambda_{0n} = \int_0^a \left[\Psi_{0n}(r) \right]^2 r \, dr = a^2 J_0 \left(\lambda_{0n} \right)^2 \tag{72}$$

TABLE V
MATERIAL PROPERTIES OF SOL-GEL $Pb\left(Zr_{0.52}Ti_{0.48}\right)O_3$

Parameter	Value
Y_p	$63 GPa$
ν_p	0.33
$d_{33,f}$	$100 pC/N$
$e_{31,f}$	varied
ϵ_{33}^{σ}	800

Values from [35].

APPENDIX C

A. Material Definition of Sol-Gel PZT

For all simulations, the material properties of the sol-gel PZT based on commonly known values found in [35] are manually input into the simulation. Material properties are defined for the stress-charge form of the piezoelectric relations [44]:

$$\sigma = c^E \varepsilon - eE$$
$$D = e\varepsilon + \epsilon^\varepsilon E \tag{73}$$

All materials including PZT are assumed to be isotropic, so the compliance matrix c^E is reduced by symmetry accordingly:

$$c^E = \begin{bmatrix} Q_{11} & Q_{12} & Q_{12} & 0 & 0 & 0 \\ Q_{12} & Q_{11} & Q_{12} & 0 & 0 & 0 \\ Q_{12} & Q_{12} & Q_{11} & 0 & 0 & 0 \\ 0 & 0 & 0 & Q_{66} & 0 & 0 \\ 0 & 0 & 0 & 0 & Q_{66} & 0 \\ 0 & 0 & 0 & 0 & 0 & Q_{66} \end{bmatrix} \tag{74}$$

where:

$$Q_{11} = \frac{Y_p(1-\nu_p)}{(1-2\nu_p)(1+\nu_p)}$$
$$Q_{12} = \frac{Y_p\nu_p}{(1-2\nu_p)(1+\nu_p)}$$
$$Q_{66} = \frac{Y_p}{2(1+\nu_p)} \tag{75}$$

with material properties defined in Table V.

Since the electric field is applied in the 3 direction and the excitation is in the 31 mode, fully defined material property matrices are unnecessary for proper simulation. Therefore, properties unnecessary for the computation, like piezoelectric constants in alternative excitation modes are filled with realistic dummy values based on [35]. To ensure that these unnecessary material constants do not affect the simulation, dummy values are swept and the results demonstrate minimal effects.

The piezoelectric constant matrix is then defined as:

$$e = \begin{bmatrix} 0 & 0 & 0 & 0 & e_{15} & 0 \\ 0 & 0 & 0 & e_{15} & 0 & 0 \\ e_{31} & e_{31} & e_{33} & 0 & 0 & 0 \end{bmatrix} \tag{76}$$

where:

$$e_{33} = d_{33,f}Q_{11}$$
$$e_{31} = e_{31,f} + \frac{Q_{12}}{Q_{11}}e_{33} \tag{77}$$

In the electric domain, the dielectric constants ϵ^ε form the matrix:

$$\epsilon^\varepsilon = \begin{bmatrix} \epsilon_{11}^\varepsilon & 0 & 0 \\ 0 & \epsilon_{22}^\varepsilon & 0 \\ 0 & 0 & \epsilon_{33}^\varepsilon \end{bmatrix} \tag{78}$$
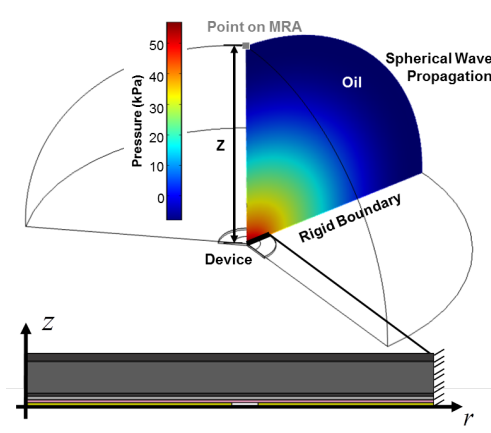
25

Fig. 16. Schematic of 2D axisymmetric pMUT COMSOL model set up showing geometry, boundary conditions and pressure measurement along the maximum response axis (MRA).

with:

$$\epsilon_{33}^{\varepsilon} = \frac{\epsilon_0 \epsilon_{33}^{\sigma} - 2d_{31}e_{31} - d_{33}e_{33}}{\epsilon_0} \tag{79}$$

where ϵ_0 is the permittivity of free space and:

$$d_{31} = \frac{1-\nu_p}{Y_p} e_{31,f}$$
$$d_{33} = d_{33,f} - \frac{2\nu_p}{1-\nu_p} d_{31} \tag{80}$$

For the above matrices, dummy values are inserted for e_{15}, $\epsilon_{11}^{\varepsilon}$, and $\epsilon_{22}^{\varepsilon}$, which in practice do not affect simulation results. However, since the modified longitudinal piezoelectric constant $d_{33,f}$ does determine the 31 mode transverse constant and the dielectric constant in 33 at constant strain, several values were inserted into simulations based on a range of anticipated values taken from [35]. Modification of $d_{33,f}$ demonstrated some effect on the broadness of the resonant peak; however, the magnitude of the effect on Q_m is limited ($< 10\%$). As such, a value consistent with [35] is selected and shown in Table V, which should provide a reasonably accurate result.

B. Single Cell Geometry

A single pMUT cell is modeled using a 2D axisymmetric piezoacoustic framework in COMSOL 4.2a. The cell is centered in a rigid wall with a length much greater than the device diameter and is surrounded on the top side by a hemispherical fluid medium. Boundary conditions are set as fixed along the plate edge, rigid on the wall and spherical wave radiation is defined at the hemispherical boundary. Pressure values as a function of distance are calculated from the mesh points along the maximum response axis (MRA), which is the axis centered and perpendicular to the active cell. The simulated model geometry and boundary conditions are depicted in Figure 16.

APPENDIX D

From Equations 59, 60, 61 and 62, initial values of the lumped parameters C_0, N^2C, L/N^2, and R/N^2 are set. Since Q_m and k_{eff}^2 are sensitive to stationary fitting and measurement conditions, error is anticipated in the initial, direct lumped parameter values. Therefore, an iterative fitting approach diagrammed in Figure 17 is adopted for determining the lumped parameter best fit. Data fit parameter values are shown in Table IV.

ACKNOWLEDGMENT

Guess:
$$k_{eff}^2(0) = 1 - \frac{f_0^2}{f_a^2}$$
$$Q_m(0) = \frac{f_0}{f'' - f'}$$

Initialize

Specify:
$$C_0 = \frac{-1}{\omega X_e}\Big|_{\omega_0}$$

$$k_{eff}^2(i) = k_{eff}^2(i-1) + \Delta k_{eff}^2$$

$$N^2 C(i) = \frac{C_0}{1 - k_{eff}(i)^2}$$

$$\frac{L}{N^2}(i) = \frac{1}{\omega_0^2 C N^2(i)}$$

$$\frac{R}{N^2}(i,j) = \frac{\omega_0}{Q_m(j)} \frac{L}{N^2}(i)$$

$$Q_m(j) = Q_m(j-1) + \Delta Q_m$$

Calculate Transfer Function

$$\left| [Dcos(2\beta)]_{exp} - [Dcos(2\beta)]_{fit} \right|^2 \to 0?$$

Stop
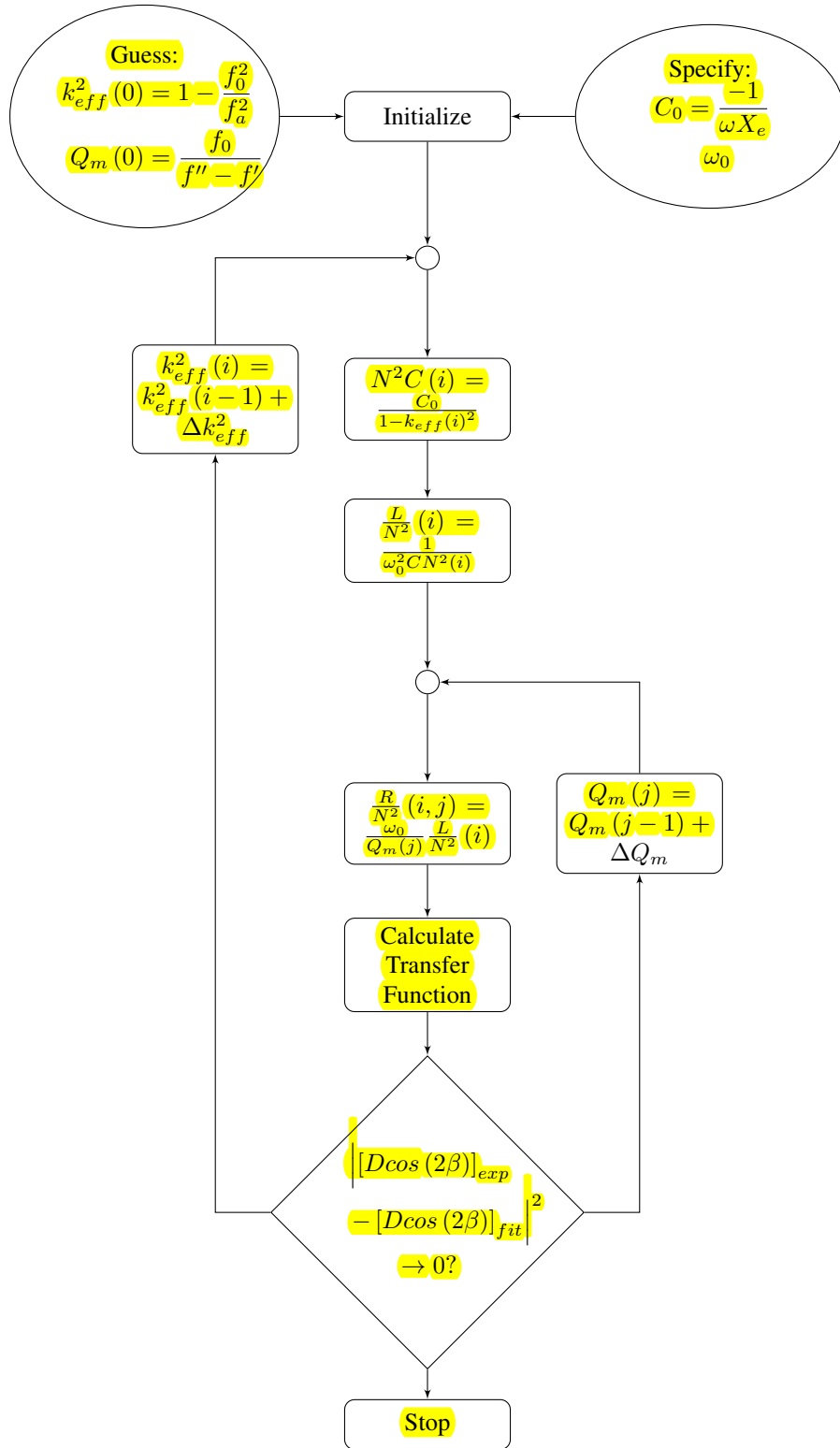
Fig. 17. Iterative lumped parameter fitting process flow. Best fit achieved with minimum residual sum of squares set by the diameter D of the motional impedance locus.

27

REFERENCES

[1] S. Shelton, M.-L. Chan, H. Park, D. Horsley, B. Boser, I. Izyumin, R. Przybyla, T. Frey, M. Judy, K. Nunan, F. Sammoura, and K. Yang, "CMOS-compatible AlN piezoelectric micromachined ultrasonic transducers," *2009 IEEE International Ultrasonics Symposium*, pp. 402–405, Sep. 2009.

[2] K. Yamashita, H. Katata, M. Okuyama, H. Miyoshi, G. Kato, S. Aoyagi, and Y. Suzuki, "Arrayed ultrasonic microsensors with high directivity for in-air use using PZT thin film on silicon diaphragms," *Sensors and Actuators A: Physical*, vol. 9798, no. 0, pp. 302–307, 2002.

[3] P. Muralt, N. Ledermann, J. Baborowski, A. Barzegar, S. Gentil, B. Belgacem, S. Petitgrand, A. Bosseboeuf, and N. Setter, "Piezoelectric micromachined ultrasonic transducers based on PZT thin films." *IEEE transactions on ultrasonics, ferroelectrics, and frequency control*, vol. 52, no. 12, pp. 2276–88, Dec. 2005.

[4] D. E. Dausch, K. H. Gilchrist, J. R. Carlson, J. B. Castellucci, D. R. Chou, and O. T. von Ramm, "Improved pulse-echo imaging performance for flexure-mode pMUT arrays," *2010 IEEE International Ultrasonics Symposium*, pp. 451–454, Oct. 2010.

[5] B. Khuri-yakub, O. Oralkan, and M. Kupnik, "Next-gen ultrasound," *IEEE Spectrum*, vol. 46, no. 5, pp. 44–54, May 2009.

[6] I. O. Wygant, X. Zhuang, D. T. Yeh, O. Oralkan, A. Sanli Ergun, M. Karaman, and B. T. Khuri-Yakub, "Integration of 2D CMUT arrays with front-end electronics for volumetric ultrasound imaging." *IEEE transactions on ultrasonics, ferroelectrics, and frequency control*, vol. 55, no. 2, pp. 327–42, Feb. 2008.

[7] B. T. Khuri-Yakub and O. Oralkan, "Capacitive micromachined ultrasonic transducers for medical imaging and therapy." *Journal of micromechanics and microengineering : structures, devices, and systems*, vol. 21, no. 5, pp. 54 004–54 014, May 2011.

[8] A. S. Savoia, G. Caliano, and M. Pappalardo, "A CMUT probe for medical ultrasonography: from microfabrication to system integration," *IEEE Transactions on Ultrasonics, Ferroelectrics and Frequency Control*, vol. 59, no. 6, pp. 1127–1138, Jun. 2012.

[9] D. Mills, "Medical imaging with capacitive micromachined ultrasound transducer (cMUT) arrays," in *IEEE Ultrasonics Symposium*, vol. 1. IEEE, 2004, pp. 384–390.

[10] Stephen D. Senturia, *Microsystem Design*, illustrate ed. Springer, 2001.

[11] P. Krulevitch, A. Lee, P. Ramsey, J. Trevino, J. Hamilton, and M. Northrup, "Thin film shape memory alloy microactuators," *Journal of Microelectromechanical Systems*, vol. 5, no. 4, pp. 270–282, 1996.

[12] A. Guedes, S. Shelton, R. Przybyla, I. Izyumin, B. Boser, and D. A. Horsley, "Aluminum nitride pMUT based on a flexurally-suspended membrane," in *Solid-State Sensors, Actuators and Microsystems Conference (TRANSDUCERS), 2011 16th International*, 2011, pp. 2062–2065.

[13] G. Perçin and B. T. Khuri-Yakub, "Piezoelectrically actuated flextensional micromachined ultrasound transducers." pp. 441–8, May 2002.

[14] G. Perçin, "Plate equations for piezoelectrically actuated flexural mode ultrasound transducers." *IEEE transactions on ultrasonics, ferroelectrics, and frequency control*, vol. 50, no. 1, pp. 81–8, Jan. 2003.

[15] F. Akasheh, "Development of piezoelectric micromachined ultrasonic transducers," *Sensors and Actuators A: Physical*, vol. 111, no. 2-3, pp. 275–287, Mar. 2004.

[16] D. E. Dausch, J. B. Castellucci, D. R. Chou, and O. T. von Ramm, "Theory and operation of 2-D array piezoelectric micromachined ultrasound transducers." *IEEE transactions on ultrasonics, ferroelectrics, and frequency control*, vol. 55, no. 11, pp. 2484–92, Nov. 2008.

[17] J. J. Bernstein, S. L. Finberg, K. Houston, L. C. Niles, H. D. Chen, L. E. Cross, K. K. Li, and E. Udayakumar, "Micromachined High Frequency Ferroelectric Sonar Transducers," *IEEE transactions on ultrasonics, ferroelectrics, and frequency control*, vol. 44, no. 5, pp. 960–969, 1997.

[18] E. Hong, S. Trolier-mckinstry, S. Member, R. Smith, S. V. Krishnaswamy, and C. B. Freidhoff, "Vibration of Micromachined Circular Piezoelectric Diaphragms," vol. 53, no. 4, pp. 697–706, 2006.

[19] F. Akasheh, J. Fraser, S. Bose, and A. Bandyopadhyay, "Piezoelectric micromachined ultrasonic transducers: modeling the influence of structural parameters on device performance," *IEEE Transactions on Ultrasonics, Ferroelectrics and Frequency Control*, vol. 52, no. 3, pp. 455–468, Mar. 2005.

[20] A. Hajati, D. Latev, D. Gardner, A. Hajati, D. Imai, M. Torrey, and M. Schoeppler, "Three-dimensional micro electromechanical system piezoelectric ultrasound transducer," *Applied Physics Letters*, vol. 101, no. 25, p. 253101, Dec. 2012.

[21] Y.-F. Wang, Y. Yang, T.-L. Ren, H. Chen, W.-J. Liao, X.-M. Kong, L.-G. Wang, C.-J. Zhou, D. Fu, and L.-T. Liu, "Ultrasonic transducer array design for medical imaging based on MEMS technologies," *2010 3rd International Conference on Biomedical Engineering and Informatics*, no. Bmei, pp. 666–669, Oct. 2010.

[22] J. Cho, M. Anderson, R. Richards, D. Bahr, and C. Richards, "Optimization of electromechanical coupling for a thin-film PZT membrane: I. Modeling," *Journal of Micromechanics and Microengineering*, vol. 15, no. 10, pp. 1797–1803, Oct. 2005.

[23] F. Sammoura and S.-G. Kim, "Theoretical modeling and equivalent electric circuit of a bimorph piezoelectric micromachined ultrasonic transducer." *IEEE transactions on ultrasonics, ferroelectrics, and frequency control*, vol. 59, no. 5, pp. 990–8, May 2012.

[24] F. Sammoura, K. Smyth, and S.-G. Kim, "Working equations of a circular multimorph piezoelectric micromachined ultrasonic transducer," in *IECON 2012 - 38th Annual Conference on IEEE Industrial Electronics Society*. IEEE, Oct. 2012, pp. 3991–3996.

[25] F. Sammoura, K. Smyth, S. Bathurst, and S.-G. Kim, "An analytical analysis of the sensitivity of circular piezoelectric micromachined ultrasonic transducers to residual stress," in *2012 IEEE International Ultrasonics Symposium*. IEEE, Oct. 2012, pp. 580–583.

[26] F. Sammoura, K. Smyth, and S.-G. Kim, "Optimizing the electrode size of circular bimorph plates with different boundary conditions for maximum deflection of piezoelectric micromachined ultrasonic transducers," *Ultrasonics*, vol. 53, no. 2, pp. 328–334, 2013.

[27] F. Sammoura, S. Akhbari, L. Lin, and S.-G. Kim, "Enhanced coupling of piezoelectric micromachined ultrasonic transducers with initial static deflection," in *2013 IEEE SENSORS*. IEEE, Nov. 2013, pp. 1–4.

[28] K. Smyth, S. Bathurst, F. Sammoura, and S.-G. Kim, "Analytic solution for N-electrode actuated piezoelectric disk with application to piezoelectric micromachined ultrasonic transducers," *IEEE Transactions on Ultrasonics, Ferroelectrics and Frequency Control*, vol. 60, no. 8, pp. 1756–1767, Aug. 2013.

[29] J. Cho, M. Anderson, R. Richards, D. Bahr, and C. Richards, "Optimization of electromechanical coupling for a thin-film PZT membrane: II. Experiment," *Journal of Micromechanics and Microengineering*, vol. 15, no. 10, pp. 1804–1809, Oct. 2005.

[30] C. Sherman and J. Butler, *Transducers and Arrays for Underwater Sound*, ser. Monograph series in underwater acoustics. Springer, 2007.

[31] P. M. C. Morse and K. U. Ingard, *Theoretical acoustics*. Princeton University Press, 1986.

[32] W. Mason, *Electromechanical transducers and wave filters*, ser. Bell Telephone Laboratories series. D. Van Nostrand Co., 1948.

[33] R. Holland, "The equivalent circuit of an N-electrode piezoelectric disk," *Proceedings of the IEEE*, vol. 54, no. 7, pp. 968–975, 1966.

[34] F. Sammoura, K. Smyth, and S.-G. Kim, "Working equations of a circular multimorph piezoelectric micromachined ultrasonic transducer," in *IECON 2012 - 38th Annual Conference on IEEE Industrial Electronics Society*. IEEE, Oct. 2012, pp. 3991–3996.

[35] P. Muralt, "PZT thin films for microsensors and actuators: Where do we stand?" *IEEE transactions on ultrasonics, ferroelectrics, and frequency control*, vol. 47, no. 4, pp. 903–15, Jan. 2000.

[36] R. L. Pritchard, "Mutual Acoustic Impedance between Radiators in an Infinite Rigid Plane," *The Journal of the Acoustical Society of America*, vol. 32, no. 6, p. 730, Jul. 1960.

[37] D. T. Porter, "Self- and Mutual-Radiation Impedance and Beam Patterns for Flexural Disks in a Rigid Plane," *The Journal of the Acoustical Society of America*, vol. 36, no. 6, p. 1154, Jul. 1964.

[38] J. Shepard, P. Moses, and S. Trolier-McKinstry, "The wafer flexure technique for the determination of the transverse piezoelectric coefficient (d31) of PZT thin films," *Sensors and Actuators A: Physical*, vol. 71, no. 1-2, pp. 133–138, Nov. 1998.

[39] F. Hunt, *Electroacoustics: the analysis of transduction, and its historical background*, ser. Harvard monographs in applied science. Harvard University Press, 1954.

[40] S. Trolier-McKinstry and P. Muralt, "Thin Film Piezoelectrics for MEMS," *Journal of Electroceramics*, vol. 12, no. 1/2, pp. 7–17, Jan. 2004.

[41] J. F. Shepard, F. Chu, I. Kanno, and S. Trolier-McKinstry, "Characterization and aging response of the d[sub 31] piezoelectric coefficient of lead zirconate titanate thin films," *Journal of Applied Physics*, vol. 85, no. 9, p. 6711, May 1999.

[42] P. Muralt and J. Baborowski, "Micromachined Ultrasonic Transducers and Acoustic Sensors Based on Piezoelectric Thin Films," *Journal of Electroceramics*, vol. 12, no. 1/2, pp. 101–108, Jan. 2004.

[43] A. Duwel, R. N. Candler, T. W. Kenny, and M. Varghese, "Engineering MEMS Resonators With Low Thermoelastic Damping," *Journal of Microelectromechanical Systems*, vol. 15, no. 6, pp. 1437–1445, Dec. 2006.

[44] T. Ikeda, *Fundamentals of Piezoelectricity*, ser. Oxford science publications. Oxford University Press, 1996.

[45] T. J. Mason, "Ultrasonics Sonochemistry Therapeutic ultrasound an overview," *Ultrasonics - Sonochemistry*, vol. 18, no. 4, pp. 847–852, 2011.

[46] Q. M. Wang, X. H. Du, B. Xu, and L. E. Cross, "Electromechanical coupling and output efficiency of piezoelectric bending actuators." *IEEE transactions on ultrasonics, ferroelectrics, and frequency control*, vol. 46, no. 3, pp. 638–46, Jan. 1999.

[47] S. H. Baek, J. Park, D. M. Kim, V. A. Aksyuk, R. R. Das, S. D. Bu, D. A. Felker, J. Lettieri, V. Vaithyanathan, S. S. N. Bharadwaja, N. Bassiri-Gharb, Y. B. Chen, H. P. Sun, C. M. Folkman, H. W. Jang, D. J. Kreft, S. K. Streiffer, R. Ramesh, X. Q. Pan, S. Trolier-McKinstry, D. G. Schlom, M. S. Rzchowski, R. H. Blick, and C. B. Eom, "Giant piezoelectricity on Si for hyperactive MEMS." *Science (New York, N.Y.)*, vol. 334, no. 6058, pp. 958–61, Nov. 2011.

[48] F. Sammoura, K. Smyth, and S. Kim, "Piezoelectric micromachined ultrasound transducer with patterned electrodes," Oct. 24 2013, uS Patent App. 13/833,159.

[49] J. Reddy, *Theory and Analysis of Elastic Plates and Shells, Second Edition*, ser. Series in Systems and Control. Taylor & Francis, 2006.

Katherine Smyth Katherine Smyth Katherine Smyth is a Ph.D. candidate in the Department of Mechanical Engineering at MIT. She received her S.B. and S.M. degrees in mechanical engineering from MIT in 2010 and 2012, respectively. Before graduate school, Katherine worked in the medical device industry as a summer intern in research and development in the 3M Drug Delivery Systems Division in 2008 and component engineering at Medtronic in 2009. Her current research interests include medical applications, and modeling and fabrication of thin film piezoelectric MEMS and nano-scale devices.

Sang-Gook Kim Sang-Gook Kim received his B.S. degree from Seoul National University, Korea, his M.S. degree from KAIST, and his Ph.d. degree from MIT. He held positions at Axiomatics Co. and Korea Institute of Science and Technology from 1986 to 1991. He joined Daewoo Corporation, Korea, in 1991 as a General Manager and then directed the Central Research Institute of Daewoo Electronics Co. as a corporate executive director before he joined MIT as a professor in 2000. His research and teaching at MIT has addressed the issues in bridging the gap between scientific findings and engineering innovations, developing novel manufacturing processes for newly developed materials, and designing and realizing new products at micro- and nano-scales. They include carbon nanotube assembly, muscle-inspired micro-actuators, nanoengineered solar cells, MEMs energy harvesters, and piezoelectric transducers. He is a fellow of the International Academy for Production Engineering (CIRP) and the American Society of Mechanical Engineers (ASME). He currently serves as the director of the Park Center for Complex Systems at MIT.